Analysis of Schwarz Waveform Relaxation for the Coupled Ekman Boundary Layer Problem with Continuously Variable Coefficients

Sophie Thery, Charles Pelletier, Florian Lemarié, Eric Blayo

ANALYSIS OF SCHWARZ WAVEFORM RELAXATION FOR THE COUPLED EKMAN BOUNDARY LAYER PROBLEM WITH CONTINUOUSLY VARIABLE COEFFICIENTS

SOPHIE THERY*, CHARLES PELLETIER†, FLORIAN LEMARIÉ‡, AND ERIC BLAYO§

Abstract. In this paper we present a global-in-time non-overlapping Schwarz method applied to the Ekman boundary layer problem. Such a coupled problem is representative of large-scale atmospheric and oceanic flows in the vicinity of the air-sea interface. Schwarz waveform relaxation (SWR) algorithms provide attractive methods for ensuring a "tight coupling" between the ocean and the atmosphere. However the convergence study of such algorithms in this context raises numerous challenges. Numerous convergence studies of Schwarz methods have been carried out in idealized settings, but the underlying assumptions to make these studies tractable may prohibit them to be directly extended to the complexity of climate models. We illustrate this aspect on the coupled Ekman problem, which includes several essential features inherent to climate modeling while being simple enough for analytical results to be derived. We investigate its well-posedness and derive an appropriate SWR algorithm. Sufficient conditions for ensuring its convergence for different viscosity profiles are then established. Finally, we illustrate the relevance of our theoretical analysis with numerical results and suggest ways to improve the computational cost of the coupling. Our study emphasizes the fact that the convergence properties can be highly sensitive to some model characteristics such as the geometry of the problem and the use of continuously variable viscosity coefficients.

Key words. Schwarz waveform relaxation, continuously variable coefficients, multiphysics coupling, coupled Ekman problem, numerical climate modeling.

AMS subject classifications. 65M55, 65F10, 65N22, 35K20, 86A08

1. Introduction.

1.1. Context and motivations. Owing to advances in computer resources and simulation tools, weather prediction systems now routinely include coupling mechanisms between several Earth system compartments; e.g. atmosphere, waves, ocean, sea-ice [4, 30]. For such applications, the coupling methods usually applied between individual compartments are ad-hoc algorithms raising synchrony issues [1, 18]. Following [17], such methods are referred to as *loose coupling methods*, since it can be shown that the coupling is relaxed to one single iteration of what should be an iterative process. Due to the overwhelming complexity of the coupling problems in the context of weather and climate, the consequences of inaccuracies in coupling algorithms on the stability and regularity of solutions are hard to untangle for realistic applications, unless a strongly coupled solution can be used as a reference. Iterative Schwarz waveform relaxation (SWR) algorithms are attractive methods for geophysical applications. Indeed, they are very weakly intrusive, can be enhanced by an appropriate choice of transmission conditions, are naturally able to handle nonconformities in time and space, and can be combined with time parallelization techniques [3, 10, 13]. However their theoretical convergence analysis is restricted to relatively simple linear model problems, often approximating space-varying quantities as constant coefficients, assuming that scalar variables are independent from each other, so that all the conditions to apply Fourier and Laplace transformations are met. As a matter of fact, coupled problems arising in Earth system modeling

*Corresponding author, Univ. Grenoble-Alpes, Inria, CNRS, Grenoble INP, LJK, Grenoble, France (sophie.thery@univ-grenoble-alpes.fr, phone : +33 4 76 63 12 63, fax : +33 4 76 61 52 52).

†Georges Lemaître Centre for Earth and Climate Research, Earth and Life Institute, UCLouvain, Louvain-la-Neuve, Belgium (charles.pelletier@uclouvain.be, phone : +32 10 47 94 36, fax : +32 10 47 94 36).

‡Univ. Grenoble-Alpes, Inria, CNRS, Grenoble INP, LJK, Grenoble, France (florian.lemarie@inria.fr, phone : +33 4 57 42 17 57, fax : +33 4 76 61 52 52).

§Univ. Grenoble-Alpes, Inria, CNRS, Grenoble INP, LJK, Grenoble, France (eric.blayo@univ-grenoble-alpes.fr, phone : +33 4 57 42 17 11, fax : +33 4 76 61 52 52).

often exhibit sharp turbulent boundary layers near the interfaces whose effect is parameterized using a spatially variable viscosity coefficient [27, 28]. The objective of this paper is to study the SWR algorithm for a model problem representative of the coupling between the turbulent oceanic and atmospheric surface boundary layers.

1.2. The coupled Ekman problem. We specifically study the so-called coupled Ekman layer problem [8], which has already been the subject of several studies by physicists and mathematicians [e.g. 5, 16, 22, 31] since it is representative of large-scale atmospheric and oceanic flows in the vicinity of the air-sea interface. So far, this type of coupled problems has been rarely studied with a focus on the numerical techniques to solve it, as proposed in the present work. The atmospheric and oceanic flows at large scale are generally represented by the primitive equations, i.e. Navier-Stokes equations written in a rotated frame under the hydrostatic assumption. Assuming that the fluid is vertically homogeneous (i.e. time and space independent density) and that horizontal velocity gradients are small compared to vertical ones, the equation for the horizontal velocity $\mathbf{U} = (u, v)$ reduces to the Reynolds averaged primitive equations:

$$\partial_t \mathbf{U} + f\mathbf{k} \times \mathbf{U} = -\partial_z \langle \mathbf{U}' w' \rangle - \rho^{-1} \boldsymbol{\nabla} p + \mathbf{F}_U \tag{1.1}$$

In (1.1), $\mathbf{k}$ is a vertical unit vector, $\langle \mathbf{U}' w' \rangle$ is the vertical component of the Reynolds stress tensor, ρ is the density, p is the corresponding hydrostatic pressure, and $\mathbf{F}_U$ contains any other forcing terms. f corresponds to the local Coriolis frequency associated with the Earth's rotation, which values typically range from $f = 0$ s^{-1} at the Equator to $f \approx \pm 1.45 \times 10^{-4}$ s^{-1} at the poles. For the $\langle \mathbf{U}' w' \rangle$ term, a common closure assumption (known as the Boussinesq hypothesis) is to consider that turbulence acts as a mixing term, thus leading to $\langle \mathbf{U}' w' \rangle = -\nu(z) \partial_z \mathbf{U}$ where ν is a so-called turbulent viscosity, much larger than the each fluid's molecular viscosities, and which varies with z [28]. Introducing the so-called stationary geostrophic velocity $\mathbf{U}_g$ defined as $-f\mathbf{k} \times \mathbf{U}_g = \rho^{-1} \boldsymbol{\nabla} p$, (1.1) becomes

$$\partial_t \mathbf{U} + f\mathbf{k} \times \mathbf{U} - \partial_z \left(\nu(z) \partial_z \mathbf{U} \right) = \mathbf{F}_U + f\mathbf{k} \times \mathbf{U}_g \tag{1.2}$$

Assuming that $\mathbf{U}_g$ is known, the problem is one-dimensional and represents the balance between the Coriolis term and the stress due to small-scale turbulent motion, under the assumption that the large-scale dynamics are in geostrophic balance. This problem typically involves boundary layers (in this context, also known as Ekman layers) which have a typical depth of tens of meters in the ocean and hundreds of meters in the atmosphere.

In the following, the physical domain of interest is $\Omega = (h_1, h_2) =]h_1, h_2[$ where $h_1 < 0 < h_2$, and $\{z = 0\}$ is the interface between two non-overlapping subdomains. The index $j \in \{1, 2\}$ is used to distinguish subdomains, T refers to the total duration of the time domain, and we consider that $\forall (a, b) \in \mathbb{R}^2$, if $a < b$ then $(a, b) =]a, b[$, else $(a, b) =]b, a[$. We note $\mathbf{U}_j = (u_j, v_j)$ the Ekman components of the velocity in subdomain $\Omega_j = (0, h_j)$, $\nu_j(z) > 0$ the turbulent viscosity, and the rhs in (1.2) is grouped as a single forcing term denoted $\mathbf{F}_j$. On the time interval $]0, T]$, the coupled Ekman boundary layer problem of interest is:

$$\partial_t \mathbf{U}_j + f\mathbf{k} \times \mathbf{U}_j - \partial_z \left(\nu_j(z) \partial_z \mathbf{U}_j \right) = \mathbf{F}_j \qquad (z, t) \in \Omega_j \times]0, T], j = 1, 2 \tag{1.3a}$$

$$\mathbf{U}_j(z, t = 0) = \mathbf{U}_{j,0}(z) \qquad z \in \Omega_j, j = 1, 2 \tag{1.3b}$$

$$\mathbf{U}_j(z = h_j, t) = \mathbf{U}_{j,g}(z = h_j) \qquad t \in [0, T], j = 1, 2 \tag{1.3c}$$

$$\nu_1(0^-) \partial_z \mathbf{U}_1(0^-, t) = \nu_2(0^+) \partial_z \mathbf{U}_2(0^+, t) \qquad t \in [0, T] \tag{1.3d}$$

$$\mathbf{U}_2(0^+, t) = \mathbf{U}_1(0^-, t) \qquad t \in [0, T] \tag{1.3e}$$

where $\mathbf{U}_{j,0}(z)$ is the initial condition, and $\mathbf{U}_{j,g}$ is the geostrophic velocity component imposed at the external boundaries of the spatial domain.

1.3. Outline of the paper. When discretizing (1.3a) in numerical models, the vertical viscosity is systematically treated implicitly in time due to the small vertical grid spacing (relative to the horizontal one) typically used in most configurations [e.g. 21]. This implicit treatment yields significant challenges in solving the coupling at a numerical level. A possibility is to consider iterative SWR methods to solve (1.3), as motivated in Sec. 1.1. The convergence properties of Schwarz algorithms with continuously variable coefficients in each subdomain have already been studied using the technique of separation of variables to decouple the space and time variables (or equivalently the two spatial variables for steady-state problems) directly in the physical space. However, previously obtained results are either restricted to cases where the coefficients vary in the direction parallel to the interface [e.g. 15], or difficult to interpret because the resulting convergence factors are given by a numerical series of abstract eigenmodes and eigenvalues [e.g. 20]. The seminal work of [24] showed, for the one-dimensional steady-state model problem $-\partial_z(\nu(z)\partial_z u) = F$, that the absorbing boundary conditions depend on the full diffusion profile and not only on its local interfacial values. In the same spirit, the aim of the present paper is to further study the effect of continuously variable coefficients on the convergence properties of SWR algorithms. We study three specific expressions of the viscosity $\nu_j(z)$, which have already been considered in the Ekman problem literature:

(i) the laminar case of [8] with constant viscosity ($\nu_j(z) = \nu_j = \text{cst}$);

(ii) in [22, 25], a more realistic case is studied by considering turbulent viscosities linearly increasing with depth (resp. with height);

(iii) in [16, 28], nearly parabolic shape functions for $\nu_j(z)$ are introduced, consistently with what is used in climate simulations.

These studies addressed exclusively physical issues, and none of them tackled the numerical resolution of the associated coupled problem.

The paper is organized as follows. The well-posedness of the coupled Ekman problem (1.3) is studied in Sec. 2, leading to a SWR algorithm being formulated. Its convergence rates for various interface conditions and viscosity profiles are determined in Sec. 3. Their asymptotic behaviour w.r.t. the parameters of the problem are investigated in Sec. 4. Finally, numerical results illustrating the relevancy of our theoretical analysis are shown in Sec. 5.

2. Formulation of the global-in-time Schwarz method and well-posedness.

2.1. Change of variables. In each medium (ocean and atmosphere), the evolution of the two velocity components, u_j and v_j, are coupled by the Coriolis term. In a matrix form, the systems (1.3a) for $j = 1, 2$ can be rewritten as:

$$\partial_t \mathbf{U}_j + \mathbf{A}\mathbf{U}_j - \partial_z\left(\nu_j(z)\,\partial_z \mathbf{U}_j\right) = \mathbf{F}_j \qquad \text{with } \mathbf{A} = \begin{pmatrix} 0 & -f \\ f & 0 \end{pmatrix} \tag{2.1}$$

These two linear PDEs can be decoupled by diagonalizing $\mathbf{A}$: $\mathbf{A} = \mathbf{P}\mathbf{D}\mathbf{P}^{-1}$ with

$$\mathbf{D} = \begin{pmatrix} if & 0 \\ 0 & -if \end{pmatrix}, \ \mathbf{P} = \frac{1}{\sqrt{2}}\begin{pmatrix} 1 & 1 \\ -i & i \end{pmatrix} \text{ and } \mathbf{P}^{-1} = \frac{1}{\sqrt{2}}\begin{pmatrix} 1 & i \\ 1 & -i \end{pmatrix}$$

Inserting this diagonalization and multiplying on the left by $\mathbf{P}^{-1}$, (2.1) becomes

$$\partial_t \mathbf{\Phi}_j + \mathbf{D}\mathbf{\Phi}_j - \partial_z\left(\nu_j(z)\,\partial_z \mathbf{\Phi}_j\right) = \mathbf{F}_j^{\Phi} \quad \text{with } \mathbf{\Phi}_j = \mathbf{P}^{-1}\mathbf{U}_j = \begin{pmatrix} \varphi_j(z,t) \\ \overline{\varphi}_j(z,t) \end{pmatrix} \tag{2.2}$$

which is equivalent to the following set of two independent scalar equations:

$$\partial_t \varphi_j + if\,\varphi_j - \partial_z\left(\nu_j(z)\,\partial_z \varphi_j\right) = F_j^{\varphi} \tag{2.3a}$$

$$\partial_t \overline{\varphi}_j - if\,\overline{\varphi}_j - \partial_z\left(\nu_j(z)\,\partial_z \overline{\varphi}_j\right) = F_j^{\overline{\varphi}} \tag{2.3b}$$

Rewritten with these new variables, the coupled Ekman layer problem (1.3) now reads:

(2.4a)
$$\partial_t \mathbf{\Phi}_j + \mathbf{D}\mathbf{\Phi}_j - \partial_z\left(\nu_j(z)\,\partial_z \mathbf{\Phi}_j\right) = \mathbf{F}_j^{\Phi} \qquad (z,t) \in \Omega_j \times]0,T]\,, j=1,2$$

$$\mathbf{\Phi}_j(z, t=0) = \mathbf{\Phi}_{\mathbf{0},j}(z) \qquad z \in \Omega_j\,, j=1,2 \tag{2.4b}$$

$$\mathbf{\Phi}_j(h_j, t) = \mathbf{\Phi}_{\mathbf{g},j}(t) \qquad t \in [0,T]\,, j=1,2 \tag{2.4c}$$

$$\mathbf{\Phi}_1(0^-, t) = \mathbf{\Phi}_2(0^+, t) \qquad t \in [0,T] \tag{2.4d}$$

$$\nu_1(0^-)\,\partial_z \mathbf{\Phi}_1(0^-, t) = \nu_2(0^+)\,\partial_z \mathbf{\Phi}_2(0^+, t) \qquad t \in [0,T] \tag{2.4e}$$

2.2. Schwarz Waveform Relaxation algorithms for the coupled Ekman problem. We consider that both submodels are independent from each other, thus prohibiting solving (2.4) with a single-model, monolithic method. Let us introduce a SWR algorithm for solving the first component of (2.4), related to variable φ. The time interval $[0,T]$ is divided into N windows $(\mathcal{T}_n)_{1\le n\le N}$, the iterative algorithm being applied successively on each window. For a given window $\mathcal{T}_n$, two sequences of sub-solutions $\left(\varphi_j^k\right)_{k\in\mathbb{N}^*, j\in\{1,2\}}$ are defined by:

$$\partial_t \varphi_j^k + \imath f \varphi_j^k - \partial_z\left(\nu_j \partial_z \varphi_j^k\right) = F_j^{\varphi} \qquad (z,t) \in (0,h_j)\times\mathcal{T}_n, j=1,2 \tag{2.5a}$$

$$\varphi_j^k\left(z, t=0_{\mathcal{T}_n}\right) = \varphi_j^{0,\mathcal{T}_n}(z) \qquad z \in (0,h_j) \tag{2.5b}$$

$$\varphi_j^k\left(z=h_j, t\right) = \varphi_{g,j}(t) \qquad t \in \mathcal{T}_n \tag{2.5c}$$

$$\mathcal{B}_{1,1}\varphi_1^k\left(0^-,t\right) = \mathcal{B}_{1,2}\varphi_2^k\left(0^+,t\right) \qquad t \in \mathcal{T}_n \tag{2.5d}$$

$$\mathcal{B}_{2,2}\varphi_2^k\left(0^+,t\right) = \mathcal{B}_{2,1}\varphi_1^{k-1}\left(0^-,t\right) \qquad t \in \mathcal{T}_n \tag{2.5e}$$

In (2.5b), $0_{\mathcal{T}_n}$ is the initial time in $\mathcal{T}_n$, and $\varphi_j^{0,\mathcal{T}_n}$ are either given by (2.4b) (if $n=1$), or by the final state φ_j^k on $\mathcal{T}_{n-1}$ (if $n \ge 2$). In the interface conditions (2.5d) and (2.5e), $\mathcal{B}_{j,l}$ are four interface operators to be chosen. The simplest choice would be $\mathcal{B}_{1,1} = \mathcal{B}_{1,2} = \mathrm{Id}$, $\mathcal{B}_{2,1} = \nu_1(0^-)\partial_z$ and $\mathcal{B}_{2,2} = \nu_2(0^+)\partial_z$, which, provided that the SWR algorithm converges, ensures that the coupling constraints (2.4d)-(2.4e) will be satisfied by the solution $(\varphi_1^\infty, \varphi_2^\infty)$. Other choices are possible to accelerate the convergence of (2.5) toward the solution of (2.4). This will be discussed in Sec. 3. We study here the "multiplicative" Schwarz method: the problem on φ_2^k is solved first, using φ_1^{k-1}; the problem on φ_1^k can then be solved.

2.3. Well-posedness. The coupled problem (1.3) is well-posed if and only if (2.4) is well-posed. We thus focus on the well-posedness of the following problem:

$$\partial_t \varphi + if\varphi - \partial_z(\nu_j(z)\partial_z\varphi) = F \qquad (z,t) \in \Omega \times [0,T] \tag{2.6a}$$

$$\varphi = g \qquad \text{on } \partial\Omega \times [0,T] \tag{2.6b}$$

$$\varphi(t=0) = \varphi_0 \qquad \text{on } \Omega \tag{2.6c}$$

[23] has shown that if $\nu(z) > 0$ is bounded in Ω, $\varphi_0 \in \mathcal{L}^2(\Omega)$, $g \in \mathcal{H}^{3/4([0,T])}$ and $F \in \mathcal{L}^2(0,T;\mathcal{L}^2(\Omega))$, then (2.6) has a unique weak solution in $\mathcal{L}^2(0,T;\mathcal{H}^1(\Omega)) \cap \mathcal{C}^0(0,T;\mathcal{L}^2(\Omega))$. The coupling algorithm (2.5) is made of successive resolutions restricted to one subdomain

(either $(h_1, 0)$ or $(0, h_2)$). A prerequisite for the well-posedness of the coupled problem is the well-posedness of subproblems, i.e. existence and uniqueness of both sub-solutions. Let us consider the generic problem:

$$\partial_t \varphi(z,t) + \imath f \varphi(z,t) - \partial_z \left(\nu(z) \partial_z \varphi(z,t)\right) = \mathcal{F}^{\varphi}(z,t) \qquad (z,t) \in (0,h) \times]0,T] \tag{2.7a}$$

$$\varphi(z, t=0) = \varphi_0(z) \qquad z \in (0,h) \tag{2.7b}$$

$$\varphi(z=h, t) = \varphi_g(t) \qquad t \in [0,T] \tag{2.7c}$$

$$\mathcal{B}\varphi(z=0,t) = G(z=0,t) \qquad t \in [0,T] \tag{2.7d}$$

where $\mathcal{B}$ is a boundary operator. If the following conditions are satisfied: (*i*) ν is bounded and strictly positive on $[0,h]$; (*ii*) $F^{\varphi} \in \mathcal{L}^2(0,T,\mathcal{L}^2(0,h))$; (*iii*) $\varphi_g(t=0) = \varphi_0(z=h)$ and $\varphi_0(t=0) = G(z=0,t=0)$; (*iv*) $\varphi_0 \in \mathcal{H}^1(0,h)$; (*v*) $\varphi_g \in \mathcal{H}^{3/4}(0,T)$; (*vi*) $G \in \mathcal{L}^2(0,T,\mathcal{H}^{3/2}(0,h)) \cap \mathcal{H}^{3/4}(0,T,\mathcal{L}^2(0,h))$; (*vii*) $\mathcal{B}$ is a Dirichlet ($\mathcal{B} = \mathrm{Id}$) or a Neumann ($\mathcal{B} = \partial_z$) operator; then (2.7) is well-posed and $\varphi \in \mathcal{L}^2(0,T,\mathcal{H}^2(0,h)) \cap \mathcal{H}^1(0,T,\mathcal{L}^2(0,h))$. If $\mathcal{B}$ is a Robin operator ($\mathcal{B} = \partial_z + r\mathrm{Id}$), the same result can be obtained by introducing further constraints (see Sec. 3.2.2). While less constraining regularity conditions guaranteeing the well-posedness of (2.7) exist (depending on $\mathcal{B}$), from now on we will assume the conditions (*i*)-(*vi*) to be satisfied, since they offer enough flexibility given our context. The well-posedness of the coupled problem and SWR algorithm applied to a similar problem with constant viscosity in each subdomain (but discontinuous at the interface) has been studied in [11]. Note that more general choices of problem unknowns and boundary operators have been applied to Schwarz algorithms and covered in existing literature [e.g., 2, 26].

3. Analytical determination of convergence rates. Setting the $\mathcal{B}_{j,l}$ operators directly from (2.4d) and (2.4e) would mean using the physical coupling operators. This has been shown to be at best suboptimal (slow SWR convergence), at worst leading to non-converging algorithms [e.g., in the case of non-overlapping domains 12]. In the following, we derive convergence rates for two different sets of boundary operators.

3.1. General form of convergence rates.

3.1.1. Ordinary differential equation on Schwarz iterate errors. A usual approach to prove the convergence of SWR algorithms is to analytically determine $e^k_{\varphi,j} = \varphi^k_j - \varphi^\star_j$, the errors between SWR iterates and the exact solution $\varphi^\star_j$. In a given time interval $]0,T]$, these errors satisfy the homogeneous Ekman problem (2.5) with homogeneous initial conditions. Results introduced in Sec. 2.3 guarantee that $e^k_{\varphi,j}$ has $\mathcal{L}^2$ space regularity in $[0,T]$. A continuous time Fourier transform can be performed, assuming that $T \to \infty$ and extending all functions to zero for $t < 0$. The problem satisfied by the errors $\widehat{e}^k_{\varphi,j}(z,\omega)$ is:

$$\imath(f+\omega)\widehat{e}^k_{\varphi,j} - \partial_z\left(\nu_j(z)\partial_z \widehat{e}^k_{\varphi,j}\right) = 0 \qquad (z,\omega) \in \Omega_j \times \mathbb{R} \tag{3.1a}$$

$$\widehat{e}^k_{\varphi,j}\left(h_j,\omega\right) = 0 \qquad \omega \in \mathbb{R} \tag{3.1b}$$

$$\mathcal{B}_{1,1}\widehat{e}^k_{\varphi,1}\left(0^-,\omega\right) = \mathcal{B}_{1,2}\widehat{e}^k_{\varphi,2}\left(0^+,\omega\right) \qquad \omega \in \mathbb{R} \tag{3.1c}$$

$$\mathcal{B}_{2,2}\widehat{e}^k_{\varphi,2}\left(0^+,\omega\right) = \mathcal{B}_{2,1}\widehat{e}^{k-1}_{\varphi,1}\left(0^-,\omega\right) \qquad \omega \in \mathbb{R} \tag{3.1d}$$

For $\omega \in \mathbb{R}$, (3.1) is a set of two linear second-order ordinary differential equations (w.r.t. z) over $\left(\widehat{e}^k_{\varphi,1}, \widehat{e}^k_{\varphi,2}\right)$. The differential operators in (3.1a) being independent of k, in each medium ($j = 1, 2$), there exists two basis functions $f_{\nu,j}(z,\omega)$ and $g_{\nu,j}(z,\omega)$ such that:

$$\widehat{e}^k_{\varphi,j}\left(z,\omega\right) = A^k_{\nu,j}(\omega)\, f_{\nu,j}(z,\omega) + B^k_{\nu,j}(\omega)\, g_{\nu,j}(z,\omega) \qquad (z,\omega) \in (0,h_j) \times \mathbb{R} \tag{3.2}$$

where $\left(A^k_{\nu,j}, B^k_{\nu,j}\right)$ is determined thanks to the boundary conditions (3.1b) and transmission conditions (3.1c) - (3.1d). In Sec. 3.3, explicit forms of the basis functions are given, for three physically meaningful forms of ν_j.

3.1.2. Convergence rate in Fourier space. The convergence rate $\rho^k_{\varphi,j}$ of the SWR algorithm (2.5) can be defined as:

$$\rho^k_{\varphi,j}(\omega) = \frac{\left|\widehat{e}^k_{\varphi,j}(z=0^{\mp},\omega)\right|}{\left|\widehat{e}^{k-1}_{\varphi,j}(z=0^{\mp},\omega)\right|} \qquad \omega\in\mathbb{R},\ k\in\mathbb{N}^*,\ j\in\{1,2\} \tag{3.3}$$

where $\mp$ depends on $j\in\{1,2\}$. $\rho^k_{\varphi,j}(\omega)$ represents the damping (or the amplification) of the error at the k^{th} SWR iteration for the ω time frequency. It can easily be shown that a sufficient condition for the convergence of the SWR algorithm is:

$$\sup_{\omega\in\mathbb{R}} \rho^k_{\varphi,j}(\omega) < 1, \qquad \forall k\in\mathbb{N}^*, \forall j\in\{1,2\} \tag{3.4}$$

since it implies that $\forall\omega\in\mathbb{R},\ \forall z\in\Omega_j,\ \widehat{e}^k_{\varphi,j}(z,\omega) \underset{k\to\infty}{\longrightarrow} 0$ for $j\in\{1,2\}$. The smaller $\rho^k_{\varphi,j}$, the faster convergence is reached. While condition (3.4) is formulated in the Fourier space, our main interest is the convergence in the physical space. Since $e^k_{\varphi,j}$ and $\widehat{e}^k_{\varphi,j}$ are continuous functions of t and ω respectively, Parseval's theorem can be used:

$$\inf_{\omega\in\mathbb{R}} \rho^k_{\varphi,j}(\omega) \le \frac{\left\|e^k_{\varphi,j}(0^{\mp},t)\right\|_2}{\left\|e^{k-1}_{\varphi,j}(0^{\mp},t)\right\|_2} = \frac{\left\|\widehat{e}^k_{\varphi,j}(0^{\mp},\omega)\right\|_2}{\left\|\widehat{e}^{k-1}_{\varphi,j}(0^{\mp},\omega)\right\|_2} \le \sup_{\omega\in\mathbb{R}} \rho^k_{\varphi,j}(\omega)\,. \tag{3.5}$$

(3.4) is therefore a sufficient condition for (2.5) to converge in the $\mathcal{L}^2$ physical space.

In practice, we are interested in the numerical solutions of the time-dependent problem (1.3) for the physical variables $\mathbf{U}_1, \mathbf{U}_2$. The error numerically observed is thus:

$$\mathbf{E}^{k,m}_j(z) = \mathbf{U}^{k,m}_j(z) - \mathbf{U}_j(z,t^m_j) \qquad 1\le m\le M_j,\ j\in\{1,2\} \tag{3.6}$$

where m is a time step index, t^m_j is the physical time corresponding to m, and M_j is the total number of time steps for the numerical approximation of $\mathbf{U}_j$ in a given time window $\mathcal{T}_n$. The associated convergence rate of (3.6) is:

$$\rho^k_{\mathbf{U}_j} = \frac{\sum_{m=1}^{M_j}\left\|\mathbf{E}^{k,m}_j(0^{\mp})\right\|_2}{\sum_{m=1}^{M_j}\left\|\mathbf{E}^{k-1,m}_j(0^{\mp})\right\|_2} \qquad k\in\mathbb{N}^*, j\in\{1,2\} \tag{3.7}$$

Using the change of variables (2.2), it is shown in App. B that:

$$\rho^k_{\mathbf{U}_j} \le \max\left\{\sup_{|\omega|\le\pi/\min\limits_{j\in\{1,2\}}\{\delta t_j\}} \rho^k_{\varphi,j}(\omega), \sup_{|\omega|\le\pi/\min\limits_{j\in\{1,2\}}\{\delta t_j\}} \rho^k_{\overline{\varphi},j}(\omega)\right\}+\epsilon \qquad k\in\mathbb{N}^*, j\in\{1,2\} \tag{3.8}$$

with $\epsilon \underset{M_j\to+\infty}{\longrightarrow} 0$. Inequality (3.8) will be used for the numerical results presented in Sec.5. In the remainder, the interval of relevant values for ω from (3.8), which depends on the time discretization, will be denoted I_ω:

$$I_\omega = \left[-\frac{\pi}{\min\limits_{j\in\{1,2\}}\{\delta t_j\}}; \frac{\pi}{\min\limits_{j\in\{1,2\}}\{\delta t_j\}}\right] = [-\omega_{\max};\omega_{\max}] \tag{3.9}$$

REMARK 1. *The upper bound (3.8) does not account for the partitioning in time windows. [14] established a link between the length of the time windows and the $\mathcal{L}^\infty$ convergence. However, this result is valid for a particular case of interface conditions with a relaxation parameter. This methodology cannot be applied here because the inverse Laplace transform of the convergence rates determined in the next subsection does not exist.*

3.2. Convergence rates for different interface conditions. We now provide exact expressions of convergence rates (3.3) for two different choices of interface operators $(\mathcal{B}_{j,l})$.

3.2.1. Dirichlet-Neumann interface conditions. Implementing a SWR algorithm with the natural Dirichlet-Neumann (DN) transmission conditions (2.4d) and (2.4e) yields choosing $\mathcal{B}_{1,1} = \mathcal{B}_{1,2} = \mathrm{Id}$, and $B_{2,j} = \nu_j\,\partial_z$. The determination of the $(A^k_{\nu,j}, B^k_{\nu,j})$ coefficients can be done by injecting the general form (3.2) for $\widehat{e}^k_{\varphi,j}$ into boundary conditions (3.1c) and (3.1d). The following convergence rate, independent of both k and j, can then be obtained:

(3.10)
$$\rho^{k,DN}_{\varphi,j} = \rho^{DN}_{\varphi} = \left| \frac{(f_2(h_2)g_2(0) - g_2(h_2)f_2(0))\,(g_1(h_1)\partial_z f_1(0) - f_1(h_1)\partial_z g_1(0))}{(f_1(h_1)g_1(0) - g_1(h_1)f_1(0))\,(g_2(h_2)\partial_z f_2(0) - f_2(h_2)\partial_z g_2(0))} \right| \frac{\nu_1(0^-)}{\nu_2(0^+)}$$

where all dependencies to ω and ν have not been explicitely written for readability. Let introduce the notations:

(3.11)
$$\mathcal{S}_1(\omega) = \frac{f_1(h_1)\,\partial_z g_1(0) - g_1(h_1)\,\partial_z f_1(0)}{f_1(h_1)\,g_1(0) - g_1(h_1)\,f_1(0)}, \qquad \mathcal{S}_2(\omega) = \frac{f_2(h_2)\,g_2(0) - g_2(h_2)\,f_2(0)}{f_2(h_2)\,\partial_z g_2(0) - g_2(h_2)\,\partial_z f_2(0)}$$

$\rho^{DN}_{\varphi}(\omega)$ can then be reformulated as:

$$\rho^{DN}_{\varphi}(\omega) = \lambda\,|\mathcal{S}_1(\omega)\,\mathcal{S}_2(\omega)|\,, \qquad \lambda = \frac{\nu_1(0^-)}{\nu_2(0^+)} \tag{3.12}$$

In the next subsections, we will give the exact expressions of $\mathcal{S}_1$ and $\mathcal{S}_2$. If $\nu_1(z)$ and $\nu_2(z)$ are of similar nature (i.e. both constant, linear or parabolic), then $\mathcal{S}_1 = \psi(h_1, \nu_1)$ and $\mathcal{S}_2 = 1/\psi(h_2, \nu_2)$,where ψ depends on the particular form of ν_j.

3.2.2. Robin-Robin interface conditions. We now consider the Robin-Robin (RR) transmission conditions:

$$\begin{array}{ll} \mathcal{B}_{1,1} = \mathrm{Id} + q\lambda\partial_z & \mathcal{B}_{1,2} = \mathrm{Id} + q\partial_z \\ \mathcal{B}_{2,2} = p\,\mathrm{Id} + \partial_z & \mathcal{B}_{2,1} = p\,\mathrm{Id} + \lambda\partial_z \end{array} \tag{3.13}$$

where $(p, q) \in \mathbb{C}^2$ are free parameters in $\mathbb{C}$, and λ is defined in (3.12). If convergence is reached, (3.13) provides the same coupled solution as the natural DN transmission conditions (2.4d)-(2.4e), while a relevant tuning of (p, q) may accelerate the SWR algorithm convergence. Note also that $p = q = 0$ corresponds to the previous case of DN conditions. In order for (2.5) to be well-posed with RR conditions, $(p, q) \in \mathbb{C}^2$ must meet $\mathrm{Re}(p) \leq 0$ and $\mathrm{Re}(q) \geq 0$. From now on, these constraints will be deemed satisfied and we will note:

$$\mathcal{P} = \left\{(p, q) \in \mathbb{C}^2,\ \mathrm{Re}(p) \leq 0 \text{ and } \mathrm{Re}(q) \geq 0\right\} \tag{3.14}$$

Similar to the DN case, the $\left(A^k_{\nu,j}, B^k_{\nu,j}\right)$ decomposition coefficients are determined using the boundary conditions (3.1b), (3.1c) and (3.1d). The resulting convergence rate for Robin-Robin conditions, written in terms of the $\mathcal{S}_j$ functions defined in (3.11), reads:

$$\rho^{RR}_{\varphi}(p, q, \omega) = \left| \frac{(\mathcal{S}_2 + q)(p + \lambda\mathcal{S}_1)}{(1 + p\mathcal{S}_2)(1 + \lambda q\mathcal{S}_1)} \right| = \rho^{DN}_{\varphi}(\omega) \left| \frac{(1 + q\mathcal{S}_2^{-1})(1 + \lambda^{-1}p\mathcal{S}_1^{-1})}{(1 + p\mathcal{S}_2)(1 + \lambda q\mathcal{S}_1)} \right| \tag{3.15}$$

Setting $p = q = 0$ in (3.15) corresponds to the DN case, i.e. $\rho_\varphi^{DN}(\omega) = \rho_\varphi^{RR}(0,0,\omega)$.

3.3. Analytical expressions of the solution for various forms of ν. We now give analytical expressions of the solutions to (3.1) for choices of $\nu(z)$ (constant, affine, and parabolic) commonly used in Earth system applications. We aim at investigating and comparing $\rho_{\mathrm{DN}}(\omega)$ and $\rho_{\mathrm{RR}}(p,q,\omega)$, for such forms of $\nu_j(z)$ assumed strictly positive and bounded in Ω_j.

REMARK 2. *As explained in Sec. 2.1, convergence rates should be studied for both φ and its complex conjugate $\overline{\varphi}$. From (2.3) and the Fourier transform properties, we can prove that:*

$$\rho_{\overline{\varphi}}^{DN}(\omega) = \rho_\varphi^{DN}(-\omega) \tag{3.16a}$$

$$\rho_{\overline{\varphi}}^{RR}(p,q,\omega) = \rho_\varphi^{RR}(\overline{p},\overline{q},-\omega) \tag{3.16b}$$

We thus restrict our study to φ, since the results on $\overline{\varphi}$ arise from (3.16b).

3.3.1. Constant viscosity. In the case $\nu_j(z) = \nu_j^c$, the basis functions (f_j, g_j) are:

$$f_j^{\mathrm{cst}}(z) = \exp\left[\chi\sqrt{\frac{f+\omega}{\nu_j^c}}z\right] \qquad \text{and} \qquad g_j^{\mathrm{cst}}(z) = \exp\left[-\chi\sqrt{\frac{f+\omega}{\nu_j^c}}z\right] \tag{3.17}$$

where $\chi = \sqrt{\imath} = e^{\imath\frac{\pi}{4}}$. Injecting (3.17) into (3.11) yields the following expressions for $\mathcal{S}_j$:

$$\mathcal{S}_1^{\mathrm{cst}} = -\chi\frac{\sqrt{\mathrm{Fo}_1}}{|h_1|}\coth\left(-\chi\sqrt{\mathrm{Fo}_1}\right), \qquad \mathcal{S}_2^{\mathrm{cst}} = -\chi^{-1}\frac{|h_2|}{\sqrt{\mathrm{Fo}_2}}\tanh\left(\chi\sqrt{\mathrm{Fo}_2}\right) \tag{3.18}$$

where the non-dimensional number $\mathrm{Fo}_j = \left(\frac{f+\omega}{\nu_j^c}\right)h_j^2$ has been introduced.

3.3.2. Affine viscosity profile. We now consider $\nu_j(z) = \nu_j^c + b_j z$ with the constraints $b_1 < 0, b_2 > 0$ leading to $\nu_j(z) > 0$ in Ω_j. The basis functions (f_j, g_j) are:

$$f_j^{\mathrm{aff}}(z) = I_0\left[2\chi\sqrt{\frac{f+\omega}{b_j^2}\nu_j(z)}\right] \qquad \text{and} \qquad g_j^{\mathrm{aff}}(z) = K_0\left[2\chi\sqrt{\frac{f+\omega}{b_j^2}\nu_j(z)}\right] \tag{3.19}$$

where I_0 and K_0 are the modified 0^{th}-order Bessel functions. Injecting (3.19) into (3.11) yields the following expressions for $\mathcal{S}_j$:

(3.20a)

$$\mathcal{S}_1^{\mathrm{aff}} = \chi\frac{\sqrt{\mathrm{Fo}_1}}{|h_1|}\frac{I_0(2\chi\sqrt{\mathrm{Fo}_1\mu_1(\mu_1+1)})\,K_1(2\chi\sqrt{\mathrm{Fo}_1}\mu_1) + K_0(2\chi\sqrt{\mathrm{Fo}_1\mu_1(\mu_1+1)})\,I_1(2\chi\sqrt{\mathrm{Fo}_1}\mu_1)}{I_0(2\chi\sqrt{\mathrm{Fo}_1\mu_1(\mu_1+1)})\,K_0(2\chi\sqrt{\mathrm{Fo}_1}\mu_1) - I_0(2\chi\sqrt{\mathrm{Fo}_1}\mu_1)\,K_0(2\chi\sqrt{\mathrm{Fo}_1\mu_1(\mu_1+1)})}$$

(3.20b)

$$\mathcal{S}_2^{\mathrm{aff}} = -\chi^{-1}\frac{|h_2|}{\sqrt{\mathrm{Fo}_2}}\frac{I_0(2\chi\sqrt{\mathrm{Fo}_2\mu_2(\mu_2+1)})\,K_0(2\chi\sqrt{\mathrm{Fo}_2}\mu_2) - I_0(2\chi\sqrt{\mathrm{Fo}_2}\mu_2)\,K_0(2\chi\sqrt{\mathrm{Fo}_2\mu_2(\mu_2+1)})}{I_0(2\chi\sqrt{\mathrm{Fo}_2\mu_2(\mu_2+1)})\,K_1(2\chi\sqrt{\mathrm{Fo}_2}\mu_2) + K_0(2\chi\sqrt{\mathrm{Fo}_2\mu_2(\mu_2+1)})\,I_1(2\chi\sqrt{\mathrm{Fo}_2}\mu_2)}$$

where μ_j is the following positive non-dimensional number:

$$\mu_j = \left|\frac{\nu_j^c}{\partial_z\nu_j(0)h_j}\right| = \frac{\nu_j^c}{b_j h_j} \tag{3.21}$$

3.3.3. Quadratic viscosity profile. In this case, we consider $\nu_j(z) = \nu_j^c + b_j z + a_j z^2$. To be consistent with the ocean-atmosphere context, we impose $a_j < 0$, $\nu_j(h_j) = \nu_j(0)$ and $\nu_j(z) > 0$ in Ω_j, which implies $\nu_j(z) = \nu_j^c - a_j h_j z + a_j z^2$. The basis functions (f_j, g_j) are:

$$f_j^{\mathrm{par}}(z) = P_{\xi_j}^0\left(\eta_j(z)\right) = {}_2F_1\left(\xi_j+1, -\xi_j, 1, \frac{1}{2} - \frac{1}{2}\eta_j(z)\right) \tag{3.22a}$$

$$g_j^{\mathrm{par}}(z) = P_{\xi_j}^0\left(-\eta_j(z)\right) = {}_2F_1\left(\xi_j+1, -\xi_j, 1, \frac{1}{2} + \frac{1}{2}\eta_j(z)\right) \tag{3.22b}$$

where $P_{\xi_j}^0$ are Legendre's functions and ${}_2F_1(a,b,c,\cdot)$ is the hypergeometric function [29]. (3.22) also introduces $\xi_j \in \mathbb{C}$ and $\eta_j(z) \in \mathbb{C}$ for $j \in \{1,2\}$, which are given in App. A. Since we assume $a_j < 0$ and $\nu_j(z) > 0$ in Ω_j, ξ_j and η_j can be simplified to:

$$\xi_j(\omega) = -\frac{1}{2}\left(1 \pm \sqrt{1 + \frac{4\imath\,(f+\omega)}{a_j}}\right) = -\frac{1}{2}\left(1 + \sqrt{1 - 4\imath\mathrm{Fo}\,\mu_j}\right) \tag{3.23a}$$

$$\eta_j(z) = \frac{\partial_z \nu_j(z)}{\sqrt{(a_j h_j)^2 - 4 a_j \nu_j^c}} \tag{3.23b}$$

where μ_j is defined like in (3.21): $\mu_j = \left|\dfrac{\nu_j^c}{\partial_z \nu(0) h_j}\right| = \dfrac{\nu_j^c}{|a_j| h_j^2}$. Computing the derivatives of the f_j^{par} and g_j^{par} functions defined in (3.22) yields the following expressions for $\mathcal{S}_j$:

$$S_1^{\mathrm{par}} = \frac{(\xi_1+1)\xi_1}{|h_1|\sqrt{1+4\mu_1}} \frac{P_{\xi_1}^0(\eta_1)G_{\xi_1}(\eta_1) + P_{\xi_1}^0(-\eta_1)G_{\xi_1}(-\eta_1)}{\left[P_{\xi_1}^0(-\eta_1)\right]^2 - \left[P_{\xi_1}^0(\eta_1)\right]^2} \tag{3.24a}$$

$$S_2^{\mathrm{par}} = \frac{|h_2|\sqrt{1+4\mu_2}}{(\xi_2+1)\xi_2} \frac{\left[P_{\xi_2}^0(-\eta_2)\right]^2 - \left[P_{\xi_2}^0(\eta_2)\right]^2}{P_{\xi_2}^0(\eta_2)G_{\xi_2}(\eta_2) + P_{\xi_2}^0(-\eta_2)G_{\xi_2}(-\eta_2)} \tag{3.24b}$$

where, for $j \in \{1,2\}$, $\eta_j = \eta_j(0) = \dfrac{(-1)^j}{\sqrt{1+4\mu_j}} = -\eta_j(H_j)$, and

$$G_{\xi_j}(\pm\eta_j) = {}_2F_1\left(\xi_j+2, 1-\xi_j, 2, \frac{1}{2} - \frac{1}{2}(\pm\eta_j)\right). \tag{3.25}$$

At this point we have prepared all the necessary ingredients to proceed to the actual convergence analysis for these three particular forms of ν_j.

4. Convergence analysis. In this section we study the behaviour of the convergence rates introduced in the previous section. In Sec. 4.1 and 4.2 we offer a review of known results on those convergence rates in specific cases, and we check that our expressions are consistent with those limit cases. Sec. 4.3 focuses on the DN case and describes the derivation of upper bounds for the convergence factor in the linear and parabolic cases. Finally, Sec. 4.4 deals with the acceleration of SWR algorithm convergence using RR interface conditions.

4.1. Overview of the results obtained in simplified cases. Existing literature has already covered different results corresponding to particular (and simplified) cases of our more general problem. These studies neglected several aspects, such as the time evolution, the Coriolis effect, the space dependency of the viscosity, or the geometry of the domain.

4.1.1. Stationary case without rotation ($\omega = 0$, $f = 0$). As emphasized by Sec. 5 of [24], in the case where $\partial_z \left(\nu(z)\partial_z\varphi\right) = 0$, it is possible to guarantee convergence of the SWR algorithm in two iterations. This result can easily be extended to the case where $\nu(z)$ is discontinuous at the interface. Using our notations, we get

$$\mathcal{S}_1^{\mathrm{sta}} = \frac{1}{\nu_1^c}\left(\int_{h_1}^{0} (\nu_1(z))^{-1} dz\right)^{-1}, \qquad \mathcal{S}_2^{\mathrm{sta}} = -\nu_2^c \left(\int_{0}^{h_2} (\nu_2(z))^{-1} dz\right) \tag{4.1}$$

with $\mathcal{S}_j^{\mathrm{sta}} = \mathcal{S}_j(\omega = 0, f = 0, \nu_j(z))$. The DN convergence factor thus reads $\rho_{\mathrm{DN}}^{\mathrm{sta}} = \lambda\, \mathcal{S}_1^{\mathrm{sta}} \mathcal{S}_2^{\mathrm{sta}}$ and the boundary conditions leading to convergence in two iterations (i.e., transparent boundary conditions) are conditions (3.13) with $p = -\lambda\, \mathcal{S}_1^{\mathrm{sta}}$ and $q = -\mathcal{S}_2^{\mathrm{sta}}$. For our three particular viscosity profiles of interest, we easily find that:

(4.2)

$$\begin{aligned}
\mathcal{S}_1^{\mathrm{sta,cst}} &= \frac{1}{|h_1|}, & \mathcal{S}_2^{\mathrm{sta,cst}} &= -h_2 \\
\mathcal{S}_1^{\mathrm{sta,aff}} &= \frac{1}{|h_1|}\,\frac{1}{\mu_1 \ln(1+1/\mu_1)}, & \mathcal{S}_2^{\mathrm{sta,aff}} &= -h_2\, \mu_2 \ln(1+1/\mu_2) \\
\mathcal{S}_1^{\mathrm{sta,par}} &= \frac{1}{|h_1|}\,\frac{\sqrt{1+4\mu_1}}{4\mu_1\ \mathrm{arccoth}\sqrt{1+4\mu_1}}, & \mathcal{S}_2^{\mathrm{sta,par}} &= -h_2\,\frac{4\mu_2\ \mathrm{arccoth}\sqrt{1+4\mu_2}}{\sqrt{1+4\mu_2}}
\end{aligned}$$

For values of the parameter μ_j smaller than 1, there is a significant impact of the spatial variations in the viscosity profile on the values of $\mathcal{S}_j^{\mathrm{sta}}$. This would affect the convergence rate in the DN case as well as the optimal coefficients in the RR one.

4.1.2. Stationary case with rotation and constant viscosity ($\omega = 0$). The values of $\mathcal{S}_j^{\mathrm{sta,cst}}$ with $f \neq 0$ can easily be derived:

$$\mathcal{S}_1^{\mathrm{sta,cst}} = \frac{1}{h_1}\chi\sqrt{\mathrm{Fo}_1^0}\coth\left(-\chi\sqrt{\mathrm{Fo}_1^0}\right), \qquad \mathcal{S}_2^{\mathrm{sta,cst}} = -h_2\frac{\tanh\left(\chi\sqrt{\mathrm{Fo}_2^0}\right)}{\chi\sqrt{\mathrm{Fo}_2^0}} \tag{4.3}$$

where $\mathrm{Fo}_j^0 = f h_j^2/\nu_j^c$ is the dimensionless number defined earlier in Sec. 3.3.1 for $\omega = 0$. In the small Fo_j^0 limit, impact of the rotation is negligible. The same remark withholds when $\mathrm{Fo}_1^0 \approx \mathrm{Fo}_2^0$ with DN interface conditions, since then $\left|\mathcal{S}_1^{\mathrm{sta,cst}}\mathcal{S}_2^{\mathrm{sta,cst}}\right| \approx \left|\mathcal{S}_{1,f=0}^{\mathrm{sta,cst}}\mathcal{S}_{2,f=0}^{\mathrm{sta,cst}}\right|$. In the general case, the rotation affects the convergence analysis only for $\mathrm{Fo}_j > 1$.

4.1.3. Nonstationary case on infinite domains without rotation and with constant viscosity ($f = 0, \nu_j(z) = \nu_j^c, |h_j| \to \infty$). This case is thoroughly studied in [9] when $\nu_1^c = \nu_2^c$, and in [19] for $\nu_1^c \neq \nu_2^c$. With DN conditions we have $\rho_{\mathrm{DN}}^{\infty,\mathrm{cst}} = \sqrt{\nu_1^c/\nu_2^c} = \sqrt{\lambda}$. The transparent conditions cannot be determined locally in time, but it is possible to optimize the (p, q) parameters in order to minimize the convergence rate over a given range of temporal frequencies $\omega \in [\omega_{\min}, \omega_{\max}]$. Such an optimization problem is analytically solved in [19]. In Sec. 5, we use those optimized transmission conditions obtained for constant viscosity in the case of non-constant viscosity profiles, and investigate their efficiency.

4.2. Consistency between the different viscosity profiles. We now promptly check that the convergence rates derived in Sec. 3 encompass the limit cases discussed in Sec. 4.1. In particular, we consider $(\omega + f) \to 0$, $\mu_j \to \infty$, and $|h_j| \to \infty$. Including the rotation (i.e. $f \neq 0$) makes the $\mathrm{Fo} = 0$ case important, since it corresponds to $\omega = -f$. In the non-rotating

case ($f = 0$), $\mathrm{Fo} = 0$ is not encountered in practice, since it only occurs when $\omega = 0$, and the stationary part of the SWR algorithm error stays at its initial state, which is zero.

4.2.1. Stationary limit without rotation ($\mathrm{Fo}_j \to 0$)**.** In the constant viscosity case, the $\mathcal{S}_j^{\mathrm{cst}}$ functions defined in (3.18) are such that we trivially find $\lim_{\mathrm{Fo}_j \to 0} \mathcal{S}_j^{\mathrm{cst}} = \mathcal{S}_{j,f=0}^{\mathrm{sta,cst}}$. For linear viscosity profiles, using Taylor expansion of Bessel functions yields:

$$\begin{array}{rcl} \lim_{\mathrm{Fo}_1 \to 0} \mathcal{S}_1^{\mathrm{aff}} & = & \frac{1}{|h_1|\,\mu_1 \ln(1+1/\mu_1)} = \mathcal{S}_{1,f=0}^{\mathrm{sta,aff}} \\ \lim_{\mathrm{Fo}_2 \to 0} \mathcal{S}_2^{\mathrm{aff}} & = & -h_2\mu_2 \ln\left(1+1/\mu_2\right) = \mathcal{S}_{2,f=0}^{\mathrm{sta,aff}} \end{array}$$

which also holds in the parabolic case.

Similarly, assuming $|h_j| \to \infty$, we recover the known results obtained under the infinite domain assumption, with and without rotation. It is worth mentioning that to maintain the consistency between the stationary and nonstationary cases for the convergence rates, we need to consider subdomains of finite sizes. Indeed considering subdomains of infinite size implies that $h_j^2 \gg \nu_j^c/(f+\omega)$, which is no longer true when $f + \omega \to 0$.

4.2.2. Small viscosity gradient limit ($\mu_j \to \infty$)**.** Since the parameters μ_j are defined as $\mu_j = \frac{\nu_j(0)}{h_j \partial_z \nu_j(0)}$, the limit case $\partial_z \nu_j(0) \to 0$ (i.e. $\mu_j \to \infty$) should lead to results similar to those obtained in the constant viscosity case. Indeed, studying $\mathcal{S}_j^{\mathrm{par}}$ and $\mathcal{S}_j^{\mathrm{aff}}$ leads to:

$$\lim_{\mu_j \to \infty} \left|\mathcal{S}_j^{\mathrm{par}}\right| = \lim_{\mu_j \to \infty} \left|\mathcal{S}_j^{\mathrm{aff}}\right| = \left|\mathcal{S}_j^{\mathrm{cst}}\right| \tag{4.4}$$

This result implies that the convergence rates are equivalent between the constant, affine and parabolic cases in the limit $\mu_j \to \infty$, whatever the interface conditions.

4.3. Behaviour of the convergence rates with DN transmission conditions. At this point we have checked that the convergence rates have the proper stationary (i.e. small Fo_j) limit and small viscosity gradients (i.e. infinite μ_j) limit. The objective is now to characterize for which parameter values the effect of a continuously variable viscosity on the convergence rate can be significant. We start with the DN case. [20] suggested that the convergence is insensitive to variations of $\nu_j(z)$ at large frequencies. Indeed, in the $\omega \to \infty$ limit, regardless of the viscosity profile, the $\mathcal{S}_1\mathcal{S}_2$ product, with $\mathcal{S}_j$ defined in either (3.18), (3.20), or (3.24), converges towards the same value $\sqrt{\nu_2^c/\nu_1^c} = \lambda^{-1/2}$. The high frequency asymptote of the DN convergence rate is thus the same as the one obtained with constant coefficients and under the infinite domain assumption. Regarding low frequencies, the stationary case discussed in Sec. 4.1 suggests that variations of the viscosity can have a large impact on the convergence rate. To further investigate this aspect, we introduce the following two quantities:

$$\mathcal{R}_j^{\mathrm{aff,cst}} = \frac{\left|\mathcal{S}_j^{\mathrm{aff}}\right|}{\left|\mathcal{S}_j^{\mathrm{cst}}\right|}, \qquad \mathcal{R}_j^{\mathrm{par,cst}} = \frac{\left|\mathcal{S}_j^{\mathrm{par}}\right|}{\left|\mathcal{S}_j^{\mathrm{cst}}\right|}$$

which are functions of the dimensionless parameters Fo_j and μ_j. In the stationary case, we had $\mathcal{R}_1^{\mathrm{aff,cst}} = \mu_1 \ln\left(1+\mu_1^{-1}\right)$ and $\mathcal{R}_1^{\mathrm{par,cst}} = 4\mu_1 \mathrm{arccoth}\left(\sqrt{1+4\mu_1}\right)(1+4\mu_1)^{-1/2}$. $\mathcal{R}_2^{\mathrm{aff,cst}}$ and $\mathcal{R}_2^{\mathrm{par,cst}}$ can be obtained by switching the respective roles of μ_1 by μ_2. Since the DN convergence rate is $\lambda|\mathcal{S}_1\mathcal{S}_2|$, the variations in the viscosity profiles on the Dirichlet side (i.e. in $(0, h_1)$) and on the Neumann side (i.e. in $(0, h_2)$) will have opposite effects in terms of convergence speed. This aspect has been already discussed earlier in the stationary case, but the same remark applies in the nonstationary case, as displayed in Fig. 4.1. Inspecting

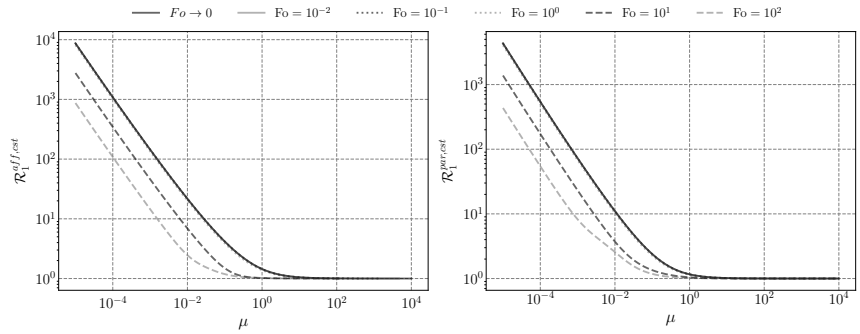

Fig. 4.1: $\mathcal{R}_1^{\mathrm{aff,cst}}$ (left) and $\mathcal{R}_1^{\mathrm{par,cst}}$ (right) with respect to μ_1, for various values of Fo_1. In particular, $\mathrm{Fo}_1 \to 0$ is represented by solid black lines, $\mathrm{Fo}_1 = 10^1$ by the dark grey dashed lines and $\mathrm{Fo}_1 = 10^2$ by the light grey dashed lines. The lines for intermediate values $\mathrm{Fo}_1 = 10^{-2}$, $\mathrm{Fo}_1 = 10^{-1}$ and $\mathrm{Fo}_1 = 10^0$ can not be distinguished from the $\mathrm{Fo}_1 \to 0$ case.

Fig. 4.1 suggests the following numerical conjectures:

$$\mathcal{R}_1^{\mathrm{aff,cst}} \leq \frac{1}{\mu_1 \ln\left(1+1/\mu_1\right)} = \frac{\mathcal{S}_1^{\mathrm{sta,aff}}}{\mathcal{S}_{1,f=0}^{\mathrm{sta,cst}}}, \qquad \mathcal{R}_2^{\mathrm{aff,cst}} \leq 1 \tag{4.5}$$

which is assumed true from now on. (4.5) leads to:

$$\rho_{\mathrm{DN}}^{\mathrm{aff}} \leq \left(\frac{\mathcal{S}_{1,f=0}^{\mathrm{sta,aff}}}{\mathcal{S}_{1,f=0}^{\mathrm{sta,cst}}}\right) \rho_{\mathrm{DN}}^{\mathrm{cst}} = \frac{\rho_{\mathrm{DN}}^{\mathrm{cst}}}{\mu_1 \ln\left(1+1/\mu_1\right)} \tag{4.6a}$$

$$\rho_{\mathrm{DN}}^{\mathrm{par}} \leq \left(\frac{\mathcal{S}_{1,f=0}^{\mathrm{sta,par}}}{\mathcal{S}_{1,f=0}^{\mathrm{sta,cst}}}\right) \rho_{\mathrm{DN}}^{\mathrm{cst}} = \frac{\sqrt{1+4\mu_1}}{4\mu_1 \operatorname{arccoth}\left(\sqrt{1+4\mu_1}\right)} \rho_{\mathrm{DN}}^{\mathrm{cst}} \tag{4.6b}$$

(4.6) contains upper bounds for the convergence rate with DN interface conditions in both the linear and parabolic viscosity cases. We now describe the derivation of an upper bound for $\rho_{\mathrm{DN}}^{\mathrm{cst}}$ to further exploit inequalities (4.6). We reformulate $\rho_{\mathrm{DN}}^{\mathrm{cst}} = \lambda |\mathcal{S}_1^{\mathrm{cst}} \mathcal{S}_2^{\mathrm{cst}}|$ as:

$$\rho_{\mathrm{DN}}^{\mathrm{cst}} = \sqrt{\lambda \frac{\mathcal{Q}(\sqrt{2\mathrm{Fo}_2})}{\mathcal{Q}(\sqrt{2\mathrm{Fo}_1})}}, \qquad \text{with } \mathcal{Q}(x) = \frac{\cosh x - \cos x}{\cosh x + \cos x}.$$

Introducing $x^{(\star,0)}$ and $x^{(\star,1)}$ the two smallest positive roots of the transcendental equation $\tanh x + \tan x = 0$ ($x^{(\star,0)} \approx 2.36502$ and $x^{(\star,1)} \approx 5.49780$), and denoting $\beta = \mathcal{Q}(x^{(\star,0)})/\mathcal{Q}(x^{(\star,1)}) \approx 1.32165$, it can then be proven (see App. C) that:

$$\begin{cases} \sqrt{\lambda/\beta} \leq \rho_{\mathrm{DN}}^{\mathrm{cst}} \leq \sqrt{\lambda \dfrac{\mathrm{Fo}_2}{\mathrm{Fo}_1}} & \text{for } \mathrm{Fo}_2 > \mathrm{Fo}_1, \\ \sqrt{\lambda \dfrac{\mathrm{Fo}_2}{\mathrm{Fo}_1}} \leq \rho_{\mathrm{DN}}^{\mathrm{cst}} \leq \sqrt{\lambda\beta} & \text{for } \mathrm{Fo}_2 \leq \mathrm{Fo}_1. \end{cases} \tag{4.7}$$

The lower bound will be used later in Sec. 4.4. Replacing $\rho_{\mathrm{DN}}^{\mathrm{cst}}$ by its upper bound in inequalities (4.6), the following result for the convergence rate in the DN case with affine viscosities

can be obtained:

$$\text{(4.8)}\qquad \begin{cases} \rho_{\mathrm{DN}}^{\mathrm{aff}} & \leq \sqrt{\lambda \dfrac{\mathrm{Fo}_2}{\mathrm{Fo}_1}}\left(\mu_1 \ln\left(1+1/\mu_1\right)\right)^{-1} & \text{for } \mathrm{Fo}_2 > \mathrm{Fo}_1, \\ \rho_{\mathrm{DN}}^{\mathrm{aff}} & \leq \sqrt{\lambda\beta}\left(\mu_1 \ln\left(1+1/\mu_1\right)\right)^{-1} & \text{for } \mathrm{Fo}_2 \leq \mathrm{Fo}_1, \end{cases}$$

Similarly, with parabolic viscosities:

$$\text{(4.9)}\qquad \begin{cases} \rho_{\mathrm{DN}}^{\mathrm{par}} & \leq \sqrt{\lambda \dfrac{\mathrm{Fo}_2}{\mathrm{Fo}_1}}\left(\dfrac{\sqrt{1+4\mu_1}}{4\mu_1\ \mathrm{arccoth}\left(\sqrt{1+4\mu_1}\right)}\right) & \text{for } \mathrm{Fo}_2 > \mathrm{Fo}_1, \\ \rho_{\mathrm{DN}}^{\mathrm{par}} & \leq \dfrac{\sqrt{\lambda\beta(1+4\mu_1)}}{4\mu_1\ \mathrm{arccoth}\left(\sqrt{1+4\mu_1}\right)} & \text{for } \mathrm{Fo}_2 \leq \mathrm{Fo}_1, \end{cases}$$

Hereafter, these upper bounds will be noted $\mathrm{U}_{\mathrm{DN}}^{\mathrm{aff}}$ and $\mathrm{U}_{\mathrm{DN}}^{\mathrm{par}}$.

So far, we have considered that ω may vary in $\mathbb{R}$. However, for a discretized problem, $\omega \in I_\omega \subsetneq \mathbb{R}$ defined in (3.9). Considering finite values of ω allows to reformulate (4.5) as

$$\mathcal{R}_1^{\mathrm{aff,cst}} \leq \mathcal{R}_1^{\mathrm{aff,cst}}(\mathrm{Fo}_1^*) \qquad \text{and} \qquad \mathcal{R}_2^{\mathrm{aff,cst}} \leq \mathcal{R}_2^{\mathrm{aff,cst}}(\mathrm{Fo}_2^*)$$

where $\mathrm{Fo}_1^* = \min\limits_{\omega\in I_\omega}(|\mathrm{Fo}_1(\omega)|) = \mathrm{Fo}_1(-f)$ and $\mathrm{Fo}_2^* = \max\limits_{\omega\in I_\omega}(|\mathrm{Fo}_2(\omega)|) = \mathrm{Fo}_2(\omega_{\max})$.

Conjecture (4.5) has been slightly relaxed to obtain more restrictive upper bounds:

$$\text{(4.10)}\qquad \rho_{\mathrm{DN}}^{\mathrm{aff}} \leq \mathrm{U}_{\mathrm{DN}}^{\mathrm{aff}}\mathcal{R}_2^{\mathrm{aff,cst}}(\omega_{\max}), \qquad \rho_{\mathrm{DN}}^{\mathrm{par}} \leq \mathrm{U}_{\mathrm{DN}}^{\mathrm{par}}\mathcal{R}_2^{\mathrm{par,cst}}(\omega_{\max})$$

where $\mathcal{R}_2^{\mathrm{aff,cst}}(\omega_{\max})$ and $\mathcal{R}_2^{\mathrm{par,cst}}(\omega_{\max})$ equal 1 for $\omega_{\max} \to \infty$, and are smaller than 1 otherwise.

To our knowledge, upper bounds similar to (4.7) had already been derived only in the case of constant coefficients and subdomains of infinite size, where it is equal to $\rho_{\mathrm{DN}}^{\infty,c} = \sqrt{\lambda}$.

4.4. Convergence analysis for RR transmission conditions. The exact transparent conditions (leading to $\rho = 0$ for all ω, hence convergence in 2 iterations) can easily be found in the Fourier space. For our model problem (2.5), considering the interface operators $\mathcal{B}_{1,1} = \mathrm{Id} + \lambda\,\Lambda_2$, $\mathcal{B}_{1,2} = \mathrm{Id} + \Lambda_2$, $\mathcal{B}_{2,1} = \Lambda_1 + \partial_z$ and $\mathcal{B}_{2,2} = \Lambda_1 + \lambda\partial_z$, convergence in 2 iterations is obtained for $\Lambda_1(\varphi_2) = \mathcal{F}^{-1}\left(-\lambda\mathcal{S}_1\widehat{\varphi}_2\right)$ and $\Lambda_2(\varphi_1) = \mathcal{F}^{-1}\left(-\mathcal{S}_2\partial_z\widehat{\varphi}_1\right)$ where $\mathcal{F}^{-1}$ denotes the inverse Fourier transform. In the stationary case ($\omega = 0$), the Λ_j operators can be found in the physical space ($\Lambda_1 = -\lambda\mathcal{S}_{1,f=0}^{\mathrm{sta}}$, $\Lambda_2 = -\mathcal{S}_{2,f=0}^{\mathrm{sta}}\partial_z$), but in the general case $\omega \neq 0$, these conditions are nonlocal in time. It nevertheless is possible to improve the convergence speed by using RR interface conditions as given in (3.13), which amounts to assimilate Λ_1 to $p\mathrm{Id}$ and Λ_2 to $q\partial_z$, with $(p,q) \in \mathcal{P}$ (see (3.14)) so that the problem is well-posed. A classical way to find suitable values for (p,q) is to solve the optimization problem:

$$\text{(4.11)}\quad \text{Find } (p^*,q^*) \in \mathcal{P} \text{ such that } \max_{\omega\in I_\omega}\rho_{\mathrm{RR}}(\omega,p^*,q^*) = \min_{(p,q)\in\mathcal{P}}\left\{\max_{\omega\in I_\omega}\rho_{\mathrm{RR}}(\omega,p,q)\right\}$$

where I_ω depends on the time discretisation. (4.11) has been analytically solved for simple cases with constant viscosity and infinite domain [9, 19]. For more complicated settings, the min-max problem can be solved numerically. In our case, with spatially-variable viscosity coefficients and bounded domains, the optimisation can only be done numerically (see Sec. 5.3 for specific examples).

We aim now at finding values of $(p,q) \in \mathcal{P}$ which would at least guarantee the convergence of the algorithm, without necessarily being the optimal choice.

Sufficient conditions on Robin coefficients to guarantee the convergence. We first recall that the convergence rate with RR interface conditions is:

$$\rho_{\mathrm{RR}}(p,q,\omega) = \left| \frac{(\mathcal{S}_2(\omega)+q)(p+\lambda\mathcal{S}_1(\omega))}{(1+p\mathcal{S}_2(\omega))(1+\lambda q\mathcal{S}_1(\omega))} \right| \tag{4.12}$$

We look for conditions on $(p,q) \in \mathcal{P} \cap \mathbb{R}^2$ such that $\rho_{\mathrm{RR}}(p,q,\omega) < 1$, which amounts to:

$$|\lambda\mathcal{S}_1\mathcal{S}_2 + \lambda q\mathcal{S}_1 + p\mathcal{S}_2 + pq|^2 < |1 + pq\lambda\mathcal{S}_1\mathcal{S}_2 + \lambda q\mathcal{S}_1 + p\mathcal{S}_2|^2 \tag{4.13}$$

It can be shown that, if $(p,q) \in \mathcal{P} \cap \mathbb{R}^2 = \mathbb{R}_- \times \mathbb{R}_+$, this is equivalent to

$$\left(\rho_{\mathrm{DN}}^2 - 1\right)(pq+1) + 2p \underbrace{\left(\mathrm{Re}\left(\lambda\mathcal{S}_1\right)|\mathcal{S}_2|^2 - \mathrm{Re}\left(\mathcal{S}_2\right)\right)}_{\vartheta_1} + 2q \underbrace{\left(\mathrm{Re}\left(\mathcal{S}_2\right)|\lambda\mathcal{S}_1|^2 - \mathrm{Re}\left(\lambda\mathcal{S}_1\right)\right)}_{\vartheta_2} < 0 \tag{4.14}$$

Assuming that $\mathcal{S}_1$ and $\mathcal{S}_2$ are such that:

$$\mathrm{Re}\left(\mathcal{S}_1\right) > 0 \qquad \text{and} \qquad \mathrm{Re}\left(\mathcal{S}_2\right) < 0, \tag{4.15}$$

then, in (4.14), $p\vartheta_1 \leq 0$ and $q\vartheta_2 \leq 0$. (4.15) can readily be analytically checked in the constant viscosity case (using $\mathcal{S}_j^{\mathrm{cst}}$ defined in (3.18)), we have only been able to numerically check it in the affine and parabolic cases (see Fig. 4.2). Assuming that (4.15) is true leads to:

$$\left\{(p,q) \in \mathbb{R}_-^* \times \mathbb{R}_+^* \text{ and } pq = -1\right\} \Rightarrow \left\{\forall\omega \in \mathbb{R},\ \rho_{\mathrm{RR}}(p,q,\omega) < 1\right\} \tag{4.16}$$

The left condition of (4.16) is not optimal in terms of convergence speed, but it does ensure that the SWR algorithm with RR interface conditions converges. We now aim at extending the 'analytically certified" region of convergence in the (p,q) space beyond the particular line $pq+1=0$. In the following we consider that property (4.15) is satisfied: this means that $p\vartheta_1 \leq 0$ and $q\vartheta_2 \leq 0$ in (4.14), and that the RR algorithm converges for $\left(\rho_{\mathrm{DN}}^2 - 1\right)(pq+1) \leq 0$. However, no conclusions can be held because the sign of $\rho_{DN}^2 - 1$ can change with respect to ω. It is nevertheless possible to determine additional constraints on (p,q), which would guarantee convergence without any assumption on the sign of $\rho_{DN}^2 - 1$. For $\omega \in \mathbb{R}$, a set of constants $(\gamma, \sigma_1, \Sigma_2) \in \mathbb{R}_+^3$ can be found such that for all $\omega \in \mathbb{R}$:

$$|\mathrm{Im}\left(\mathcal{S}_j(\omega)\right)| \leq \gamma\,|\mathrm{Re}\left(\mathcal{S}_j(\omega)\right)| \qquad \text{for } j \in \{1,2\}, \tag{4.17}$$

$$|\mathrm{Re}\left(\mathcal{S}_1(\omega)\right)| \geq \sigma_1 \qquad \text{and} \qquad |\mathrm{Re}\left(\mathcal{S}_2(\omega)\right)| \leq \Sigma_2 \tag{4.18}$$

Again, this can be analytically proved in the constant viscosity case, but has only been numerically checked in the affine and parabolic cases. Under the (4.17) and (4.18) hypotheses, sufficient conditions to satisfy (4.14) are:

$$q \geq \frac{1+\gamma^2}{2}\Sigma_2 \qquad \text{and} \qquad |p| \leq 2\lambda\sigma_1. \tag{4.19}$$

Restricting the study to $\omega \in I_\omega$ yields the following two additional constraints:

$$|\mathrm{Re}\left(\mathcal{S}_1(\omega)\right)| \leq \Sigma_1 \qquad \text{and} \qquad |\mathrm{Re}\left(\mathcal{S}_2(\omega)\right)| \geq \sigma_2 \tag{4.20}$$

where $(\Sigma_1, \sigma_2) \in {\mathbb{R}_+}^2$ are constant. Under the (4.17), (4.18) and (4.20) hypotheses, we find another sufficient condition for ensuring (4.14):

$$q \leq 2\sigma_2 \qquad \text{and} \qquad |p| \geq \frac{1+\gamma^2}{2}\lambda\Sigma_1 \tag{4.21}$$

To complete the study, we express the constraints (4.19) and (4.21) on (p,q) in terms of model parameters.

Determination of γ, σ_j and Σ_j in the constant viscosity case. In App. C, we prove that for $\omega \in \mathbb{R}$, $|\mathcal{S}_1^{\rm cst}| \geq \left|\mathcal{S}_{1,f=0}^{\rm sta,cst}\right| = \frac{1}{|h_1|}$ and $|\mathcal{S}_2^{\rm cst}| \leq \mathcal{S}_{2,f=0}^{\rm sta,cst} = |h_2|$. This yields to $\sigma_1^{\rm cst} = \left(\sqrt{1+\gamma^2}\,|h_1|\right)^{-1}$ and $\Sigma_2^{\rm cst} = |h_2|$. The value of γ in (4.17) can be accurately determined in the constant viscosity case (see App. C):

$$\gamma^{\rm cst} = \frac{\sinh(y^{(\star,0)}) - \sin(y^{(\star,0)})}{\sinh(y^{(\star,0)}) + \sin(y^{(\star,0)})} \approx 1.0573 \tag{4.22}$$

with $y^{(\star,0)}$ the smallest positive root of $\tanh(y) - \tan(y) = 0$. Now that appropriate values of $\gamma^{\rm cst}$, $\Sigma_2^{\rm cst}$ and $\sigma_1^{\rm cst}$ have been found, (4.19) can be adapted to provide the following sufficient condition on (p,q) ensuring the convergence of the SWR algorithm with constant viscosities:

(4.23)
$$q \geq \frac{1+\left(\gamma^{\rm cst}\right)^2}{2}\,|h_2| = 1.05894\,\mathcal{S}_{2,f=0}^{\rm sta,cst}, \quad \text{and} \quad |p| \leq \frac{1}{\sqrt{1+\left(\gamma^{\rm cst}\right)^2}}\,\frac{\lambda}{|h_1|} = 1.3944\,\lambda\,\mathcal{S}_{1,f=0}^{\rm sta,cst}$$

Condition (4.20) is not satisfied by the full continuous problem, but only by its semi-discretized in time version, where $|\omega| \leq \omega_{\max}$. In this case, appropriate values of $\sigma_2^{\rm cst}$ and $\Sigma_1^{\rm cst}$ in (4.20) are respectively $\sigma_2^{\rm cst} = |\mathcal{S}_2^{\rm cst}(\omega_{\max})|\,/\sqrt{1+\gamma^2}$ and $\Sigma_1^{\rm cst} = |\mathcal{S}_1^{\rm cst}(\omega_{\max})|$. Based on (4.21), the following sufficient condition for convergence can be found:
(4.24)
$$q \leq \frac{|\mathcal{S}_2^{\rm cst}(\omega_{\max})|}{\sqrt{1+\left(\gamma^{\rm cst}\right)^2}} = 1.3944\,\left|\mathcal{S}_2^{\rm cst}(\omega_{\max})\right|, \quad \text{and} \quad |p| \geq \frac{1+\left(\gamma^{\rm cst}\right)^2}{2}\left|\mathcal{S}_1^{\rm cst}(\omega_{\max})\right| = 1.05894\,\left|\mathcal{S}_1^{\rm cst}(\omega_{\max})\right|$$

Interestingly, the choice of Robin parameters providing the exact transparent conditions in the stationary case (i.e. $q_0 = |h_2|$ and $p_0 = -\lambda/|h_1|$) leads to $\rho_{\rm RR}(\omega, p_0, q_0) < 1$.

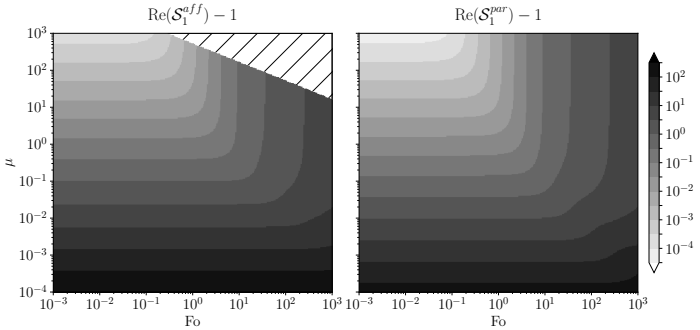

Fig. 4.2: $\mathcal{S}_1^{\rm aff} - 1$ (left) and $\mathcal{S}_1^{\rm par} - 1$ (right) with respect to Fo and μ. Note that both axes and the colorbar are in logarithmic scale. The hatched area corresponds to values of (Fo, μ) for which the computations of Bessel functions in $\mathcal{S}_1^{\rm aff}$ suffer from numerical instability.

Determination of γ, σ_j and Σ_j in the affine and parabolic cases. As soon as the viscosity profiles are no longer constant, properties (4.15), (4.17), and (4.18) can only be numerically assessed. From Fig. 4.2 we can conjecture that $\mathrm{Re}(\mathcal{S}_1^{\rm aff}) \geq 1$ (resp. $\mathrm{Re}(\mathcal{S}_1^{\rm par}) \geq 1$), which suggests that (4.15) and (4.17) on $\mathcal{S}_1$ are satisfied. Since $\mathcal{S}_2(\mu, \mathrm{Fo}) = -|h_2|/(|h_1|\mathcal{S}_1(\mu, \mathrm{Fo}))$, this would imply that (4.15) and (4.17) are also satisfied for $\mathcal{S}_2$. Moreover, if we restrict the

variations of ω to I_ω (i.e. $\mathrm{Fo} \in [\mathrm{Fo}(-\omega_{\max}), \mathrm{Fo}(\omega_{\max})]$) we can speculate from Fig. 4.2 that (4.20) is also satisfied with variable viscosity profiles. Fig. 4.3 shows numerical values of $\log_{10}(\gamma)$ (with γ defined in (4.17)) in the affine and parabolic cases; it is in agreement with the conjecture that they do not significantly depart from the value analytically found in the constant viscosity case. Assuming that γ is the same as the one found analytically in previous paragraph, the following conjectures can be proposed:

$$\sigma_1^{\mathrm{aff}} = \frac{\left|\mathcal{S}_{1,f=0}^{\mathrm{sta,aff}}\right|}{\sqrt{1+\left(\gamma^{\mathrm{cst}}\right)^2}} \qquad \text{and} \qquad \Sigma_2^{\mathrm{aff}} = \left|\mathcal{S}_{2,f=0}^{\mathrm{sta,aff}}\right| \tag{4.25}$$

The same holds in the parabolic case. As in the constant viscosity case, condition (4.20) is only available for the discrete in time problem and we can conjecture that:

$$\sigma_2^{\mathrm{aff}} = \frac{\left|\mathcal{S}_2^{\mathrm{aff}}(\omega_{\max})\right|}{\sqrt{1+\left(\gamma^{\mathrm{cst}}\right)^2}} \qquad \Sigma_1^{\mathrm{aff}} = \left|\mathcal{S}_1^{\mathrm{aff}}(\omega_{\max})\right|$$

which is valid also in the parabolic case. The relevance of these conditions will be illustrated with some numerical examples in Sec. 5. As in the constant viscosity case, the Robin parameters corresponding to the exact transparent conditions in the stationary case, i.e. $q_0 = -\mathcal{S}_{2,f=0}^{\mathrm{sta,aff}}$ (resp. $= -\mathcal{S}_{1,f=0}^{\mathrm{sta,par}}$) and $p_0 = -\lambda\mathcal{S}_{1,f=0}^{\mathrm{sta,aff}}$ (resp. $= -\lambda\mathcal{S}_{1,f=0}^{\mathrm{sta,par}}$), lead to a convergent algorithm.

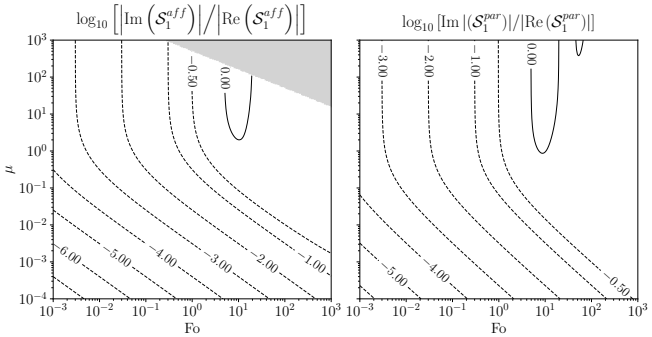

Fig. 4.3: Left: $\log_{10}\left[\left|\mathrm{Im}\left(\mathcal{S}_1^{\mathrm{aff}}\right)\right|/\left|\mathrm{Re}\left(\mathcal{S}_1^{\mathrm{aff}}\right)\right|\right]$; right: $\log_{10}\left[\left|\mathrm{Im}\left(\mathcal{S}_1^{\mathrm{par}}\right)\right|/\left|\mathrm{Re}\left(\mathcal{S}_1^{\mathrm{par}}\right)\right|\right]$ with respect to Fo and μ (both axes are in logarithmic scale). The grey area corresponds to values of (Fo, μ) for which the computations of $\mathcal{S}_1^{aff}$ suffer from numerical instability (in the Bessel function evaluation).

5. Numerical experiments. In this section, we illustrate the different properties highlighted in the previous sections with numerical experiments. In particular, we numerically investigate the influence of continuously variable coefficients on the convergence in the case of DN and RR interface conditions in view of our theoretical results. We directly simulate the equations for the errors, i.e. we set $\mathbf{F}_1 = \mathbf{F}_2 = 0$, $\mathbf{U}_{1,g} = \mathbf{U}_{2,g} = 0$ in (1.3).

5.1. Discretization. Because viscosity coefficients $\nu(z)$ can have large variations in space, we use a nonuniform grid with increased resolution in the vicinity of the interface. On subdomain Ω_j of length $|h_j|$, the location of the cell center z_k for grid cell k is

$$z_k = h_c\sigma_k + (|h_j| - h_c)\frac{\sinh(\sigma_k\theta_s)}{\sinh\theta_s}, \qquad \sigma_k = \frac{k}{N}, \qquad k = 0, \ldots, N$$

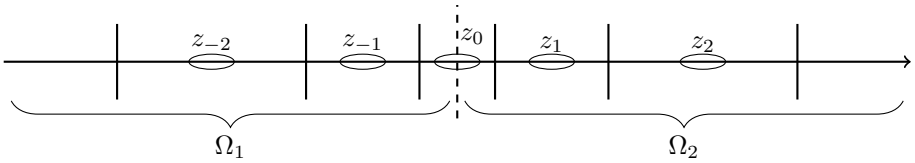

Fig. 5.1: Grid arrangement for the discretization of model problem (1.3) on subdomains Ω_1 and Ω_2. Vertical lines indicate interfaces between grid cells while ellipses indicate cell centers. The vertical dashed line represents the interface between Ω_1 and Ω_2.

with $N+1$ the number of grid points for the discretization on Ω_j, and (h_c, θ_s) two parameters controlling the grid stretching. For our experiments, we choose $h_c = 10^{-3}|h_j|$, $\theta_s = 10^{-1}N$ and $N \gg 10$, which leads to a resolution of $\Delta z \approx 10^{-3}|h_j|$ near the interface and $\Delta z \approx 10^{-1}|h_j|$ near the external boundaries. As shown in Fig. 5.1, the interface is located in the middle of a grid cell at $z_0 = 0$. Regarding the discretization in time, in order to circumvent the stability issues of the Euler forward scheme to integrate the Coriolis term in (1.3), a Forward-Backward approach is used. For a velocity vector $\mathbf{U} = (u, v)$, this scheme reads:

$$u_k^\star = u_k^n + \Delta t\ f v_k^n \qquad\qquad v_k^\star = v_k^n - \Delta t\ f u_k^\star$$

the order of integration of u and v being inverted from one time-step to the other to minimize splitting errors. The diffusion is then discretized using a standard implicit finite-difference scheme. This leads to a tridiagonal system for interior grid points, which reads (for u):

$$a_k u_{k-1}^{n+1} + b_k u_k^{n+1} + c_k u_{k+1}^{n+1} = u_k^\star \qquad k = 1, \dots, N-1$$

where $a_k = -\dfrac{\nu_{k-1/2}\,\Delta t}{\Delta z_k \Delta z_{k-1/2}}$, $c_k = -\dfrac{\nu_{k+1/2}\,\Delta t}{\Delta z_k \Delta z_{k+1/2}}$, and $b_k = 1 - a_k - c_k$, with $\Delta z_k = z_{k+1/2} - z_{k-1/2}$ and $\Delta z_{k+1/2} = z_{k+1} - z_k$. Same applies to the v velocity component.

Since the interface is located at a cell center (Fig. 5.1), the evaluation of the gradient $(\partial_z u)_0$ at the interface (required for Neumann and Robin conditions) is obtained via extrapolation with a second-order formula. Simulations have been performed using a multiplicative Schwarz algorithm initialized with a random guess at the interface, so that the observed error widely samples the temporal frequencies that can be represented by the computational grid.

5.2. Numerical experiments for Dirichlet-Neumann interface conditions. We compare the theoretical convergence rate $\rho_\varphi(\omega)$ on I_ω, with the observed one $\rho_{\mathbf{U}}^k(z=0)$ defined in (3.7), for the three viscosity profiles, and for fixed parameters h_j, ν_j^c and $\partial_z \nu_j(0)$. This comparison is illustrated by Fig. 5.2 and 5.3. The left panels represent the theoretical convergence rates $\rho_{\mathrm{DN}}^{\mathrm{cst}}(\omega)$, $\rho_{\mathrm{DN}}^{\mathrm{aff}}(\omega)$ and $\rho_{\mathrm{DN}}^{\mathrm{par}}(\omega)$ for different parameter values, and the convergence rates obtained from numerical simulations. Since the latter vary from one Schwarz iteration to the next one, they are not restricted to a single line but are materialized by a shaded area delimited by the minimum and maximum observed values over I_ω. Since we consider $f \neq 0$, the theoretical convergence rates are not symmetrical with respect to $\omega = 0$, hence the figures feature two curves for each rates: one for $\rho_\varphi(\omega > 0)$ and one for $\rho_\varphi(\omega < 0)$, with $|\omega|$ as the x-axis. Several remarks can be drawn. First, the numerically observed convergence rates satisfy the theoretical bound given by (3.8). Indeed, the maximum of the curves is systematically above the grey shaded areas, which are bounded by $\min_k \rho_{\mathbf{U}_2}^k(z=0)$ and $\max_k \rho_{\mathbf{U}_2}^k(z=0)$ (where k is the iteration number). As expected, the convergence (or divergence) of the SWR

algorithm depends on both the physical configuration and the nature of the viscosity profile (constant, affine or parabolic). For instance, as shown in the right panels of Fig. 5.2 and 5.3, there are situations where the algorithm converges only for the constant viscosity case and diverges in the affine and parabolic cases (while the exact opposite behaviour can be found for other parameter values). These examples illustrate that the spatial variations of the diffusion coefficient is determining for the SWR algorithm convergence, and that results from one particular choice cannot be generalized to other ones.

Fig. 5.3 confirms the consistency between the numerically observed convergence rate, computed in the physical space, and the theoretical convergence rate, computed in the Fourier space. The observed convergence rates (right panel) are smaller during the first iterations. This is due to the rapid damping of error components corresponding to the frequencies with fast convergence. As iterations progress, the errors at slower-converging frequencies have more influence on the $\mathcal{L}^2$ norm, and thus on the observed convergence rate. This results in an observed convergence rate which increases as a function of the iteration number. Consistently, when the variations of the theoretical convergence rate in the Fourier space are small, the observed convergence rate is more stable during the iterations. Fig.5.3 also shows that the peak corresponding to $\omega + f = 0$ in the theoretical convergence rates indeed impacts the convergence at a numerical level. Such peak appears in the theoretical derivation only when considering finite size domains and including the Coriolis effect. Without these two hypotheses, the curve for the convergence rate would be flat, corresponding to $\rho(\omega > 0)$. This example illustrates that the observed convergence rate is larger than the one given by the flat portion of the theoretical convergence rate, because its maximum value is influenced by the asymptotic case $\omega + f \to 0$.

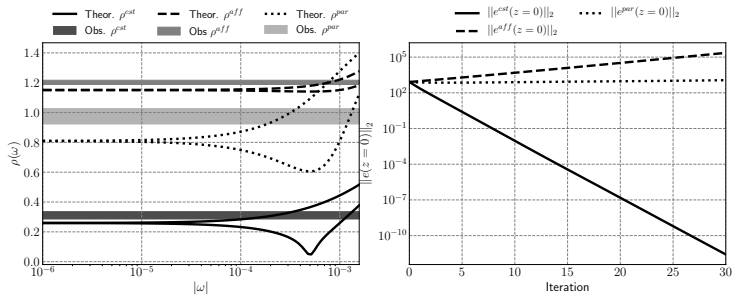

Fig. 5.2: Left panel: convergence rates with respect to $|\omega| \leq \pi/\Delta t$ for three different viscosity profiles: constant (solid lines), parabolic (dotted lines) and affine (dashed lines). The two curves correspond to the theoretical convergence rate $\rho(\omega > 0)$ and $\rho(\omega < 0)$. The grey areas correspond to the values reached by the observed convergence rate in $\mathcal{L}^2$ norm. Right panel: $\mathcal{L}^2$ norm of the error on $(u, v)(z = 0)$ as a function of the iteration number. The parameter values are: $h_1 = -200\,\mathrm{m}$, $\nu_1^c = 0.6\,\mathrm{m^2\,s^{-1}}$, $\partial_z \nu_1(0) = 0.4\ \mathrm{m\,s^{-1}}$, $h_2 = 18.0\,\mathrm{m}$, $\nu_2^c = 1.2\,\mathrm{m^2\,s^{-1}}$, $\partial_z \nu_2(0) = 0.01\,\mathrm{m\,s^{-1}}$, $f = 5 \times 10^{-4}\,\mathrm{s^{-1}}$, $\Delta t = 2000\,\mathrm{s}$.

5.3. Numerical experiments for Robin-Robin interface. Here we focus on the calculation of Robin coefficients for optimizing the SWR algorithm convergence, as explained in Sec. 4.4. Many studies have already determined the optimized coefficients in various cases with infinite domain and without Coriolis effect [e.g. 9, 10, 19]. The assumptions made during their determination may lead to such coefficients being irrelevant in the cases investigated below. In Fig. 5.4, the behaviour of the SWR algorithm for a parabolic profile is shown, with

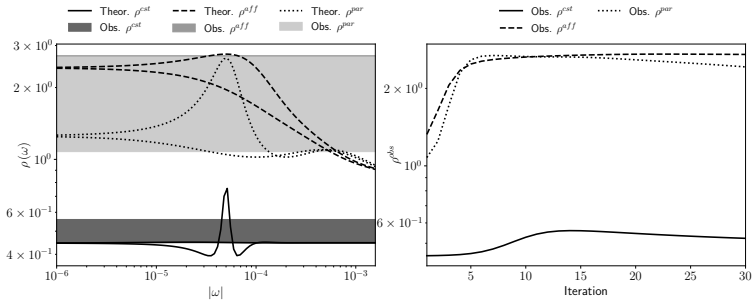

Fig. 5.3: Left panel: same as left panel of Fig. 5.2 but for different parameter values. Right panel: observed convergence rates in $\mathcal{L}^2$ norm on $(u, v)(z = 0)$ as a function of the iterations. The parameter values are: $h_1 = -50\,\mathrm{m}$, $\nu_1^c = 0.012\,\mathrm{m^2\,s^{-1}}$, $\partial_z \nu_1(0) = -0.04\,\mathrm{m\,s^{-1}}$, $h_2 = 200\,\mathrm{m}$, $\nu_2^c = 0.06\,\mathrm{m^2\,s^{-1}}$, $\partial_z \nu_1(0) = 0.01\,\mathrm{m\,s^{-1}}$, $f = 5 \times 10^{-5}\,\mathrm{s^{-1}}$ and $\Delta t = 2000\,\mathrm{s}$. Note that the y-axis scale is logarithmic.

four different choices of Robin coefficients: (*i*) optimized coefficients analytically determined in [19] for infinite domain, constant viscosity and no Coriolis term (the corresponding convergence rate will be referred to as $\rho_0^{\mathrm{RR,par}}$); (*ii*) (resp. (*iii*) and (*iv*)) coefficients numerically optimized by solving the min-max problem (4.11) on $\rho_{\mathrm{RR}}^{\mathrm{cst}}$ (resp. $\rho_{\mathrm{RR}}^{\mathrm{aff}}$ and $\rho_{\mathrm{RR}}^{\mathrm{par}}$) (the convergence rate is noted $\rho_1^{\mathrm{RR,par}}$ (resp. $\rho_2^{\mathrm{RR,par}}$ and $\rho_3^{\mathrm{RR,par}}$)). As in the DN case, the numerically observed convergence rates agree well with the theoretical bound given by (3.8). Fig. 5.4a displays the theoretical convergence rates $\rho_s^{\mathrm{RR,par}}$ $(s \in \{0 \dots 3\})$. This figure clearly illustrates the fact that a significant gain in performance can be obtained when optimizing the Robin coefficients using a convergence rate as consistent as possible with the practical problem of interest. As confirmed by the experiments shown in Fig. 5.4b, optimizing the Robin coefficients using a convergence rate which accounts for the parabolic viscosity profile, finite size subdomains and the Coriolis effect provides a very efficient algorithm. On the contrary, other alternatives where simplifications have been made are at best suboptimal, and may even lead to divergence. Once again, neglecting the variations of the viscosity in the convergence analysis can conduct to a critically erroneous choice of Robin coefficients.

Besides the determination of optimized Robin coefficients, Sec. 4.4 dealt with different ways of choosing acceptable coefficients without numerically solving the costly (4.11) min-max problem. Fig. 5.5 maps the maximum (w.r.t. ω) of the convergence rate as a function of $p < 0$ and $q > 0$, for the three types of viscosity profiles of interest, with specific symbols localizing the four different couples of (p, q) values discussed in previous paragraph, and used in Fig. 5.4. (p, q) values corresponding to optimized parameter values in the nonrotating and stationary case (i.e., $p_0 = -\lambda \mathcal{S}_{1,f=0}^{\mathrm{sta,par}}$ and $q_0 = -\mathcal{S}_{2,f=0}^{\mathrm{sta,par}}$), are also displayed. The upper left panel of Fig. 5.5 underlines that using Robin coefficients obtained from optimizing the constant or affine viscosity case does not ensure good convergence of the model with a parabolic viscosity profile. The white zones correspond to areas delimited by the sufficient conditions (4.19) and (4.21), which ensure algorithm convergence, with γ being numerically determined from the non-constant viscosity profiles. As explained in Sec. 4.4, the (p_0, q_0) couple from the nonrotating and stationary case is located close to the white zone, which ensures convergence for all three viscosity profiles without requiring solving a costly optimization problem.

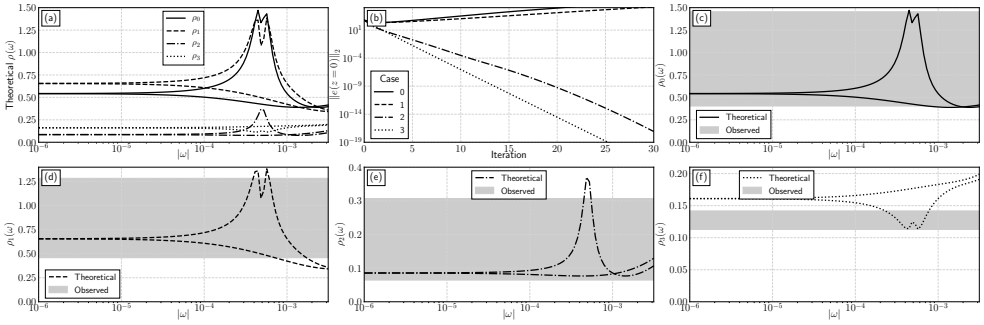

Fig. 5.4: (a): Theoretical convergence rate with respect to $|\omega| \leq \pi/\Delta t$ for a given parabolic viscosity profile. The four couples of curves correspond to different choices of Robin coefficients (see Sec. 5.3). (b): Evolution of the $\mathcal{L}^2$-norm of the error on $(u, v)(z = 0)$ with respect to the iterations for numerical simulations in the same setting as reported in (a). (c)-(f): details of the four cases from (a), one by one. Grey zones correspond to the amplitude of the values reached by the observed convergence rate over the iterations and the temporal frequencies. Parameter values are: $h_1 = -50\,\mathrm{m}$, $\nu_1^c = 0.06\,\mathrm{m^2\,s^{-1}}$, $\partial_z \nu_1(0) = -0.001\,\mathrm{m\,s^{-1}}$, $h_2 = 200\,\mathrm{m}$, $\nu_2^c = 0.012\,\mathrm{m^2\,s^{-1}}$, $\partial_z \nu_2(0) = 0.04\,\mathrm{m\,s^{-1}}$, $f = 5 \times 10^{-4}\,\mathrm{s^{-1}}$, $\Delta t = 1000\,\mathrm{s}$.

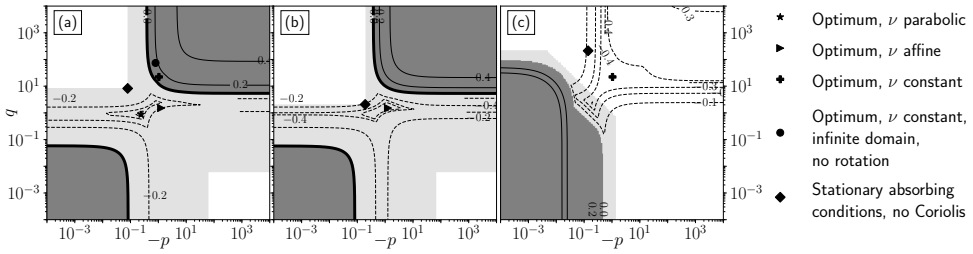

Fig. 5.5: Contour lines: $\max_\omega \log_{10} \rho_{\mathrm{RR}}(\omega)$ with respect to $(-p, q) \in \mathbb{R}_+^2$ for different viscosity profiles: (a) parabolic; (b) affine; (c) constant. White zones correspond to convergence guaranteed by (4.19) and (4.21); light grey zones to observed convergence without having those conditions satisfied; dark grey zones to divergence. The first four symbols correspond to the values of (p, q) used in Fig. 5.4. The fifth symbol corresponds to (p_0, q_0) obtained in the stationary case without rotation (Sec. 4.4). The parameter values are those of Fig. 5.4.

6. Conclusion. In this paper, we have analyzed the convergence of global-in-time Schwarz waveform relaxation (SWR) algorithms on the coupled Ekman layer problem with continuously variable viscosity coefficients. We have obtained new theoretical results for problems featuring several delicacies which are very often neglected in existing convergence analyses: viscosity profiles are allowed to vary in space and the Coriolis effect associated with the Earth's rotation is accounted for. First, we have emphasized that including the Coriolis effect amounts to investigating a reaction-diffusion equation in the complex space. We then have considered two types of SWR interface conditions (Dirichlet-Neumann (DN) and Robin-Robin (RR)), and three types of viscosity profiles (constant, affine and parabolic). Fourier space convergence rates have been given for all three cases, with indications on how such results are linked to empirical convergence rates observed from numerically simulated problems. In our physically realistic setting, we have defined analytical bounds of SWR con-

vergence rate for constant viscosity profiles for the DN interface conditions, while for the RR case we have conjectured sufficient conditions ensuring convergence. Similar results extended to the affine and parabolic viscosity cases have also been numerically assessed. More importantly, we have emphasized that spatial variations in viscosity can be determining on the convergence of SWR algorithm, and that neglecting them can mislead preliminary convergence analyses.

This work is part of a community effort to mathematically and numerically evaluate the coupling methods presently used in realistic climate models. Several open perspectives are left. First, some of this work's conclusions rely on numerical conjectures that have not been proved, but only observed. Second, generalizing our study to cubic viscosity profiles would be interesting, as this would include the profile proposed by [28] which is used as a baseline in some broadly-used turbulence schemes. In the same way as Bessel (resp. hypergeometric) functions are used for describing SWR algorithm solutions for affine (resp. parabolic) viscosity profiles, Heun's function is a good candidate for studying the cubic case. However, preliminary numerical studies have suffered from numerical instabilities arising from evaluating such functions.

On the longer term, a significant challenge would be to investigate SWR algorithms in the context of viscosity profiles resulting from a turbulent kinetic energy (TKE) closure. Such methods, which are broadly used in climate models, rely on solving an additional prognostic equation and result in space and time varying viscosity profiles depending nonlinearly on model variables. Investigating idealized testcases, for which such an approach can be fruitful, are a necessary and instructive endeavor for better understanding the numerics of asynchronous model coupling.

Acknowledgements. The authors acknowledge the support of the French national research agency (ANR) through contract ANR-16- CE01-0007.

References.

[1] A. BELJAARS, E. DUTRA, G. BALSAMO, AND F. LEMARIÉ, *On the numerical stability of surface–atmosphere coupling in weather and climate models*, Geosci. Model Dev., 10 (2017), pp. 977–989.

[2] D. BENNEQUIN, M. J. GANDER, AND L. HALPERN, *Optimized Schwarz Waveform Relaxation Methods for Convection Reaction Diffusion Problems*, tech. report, 2004-24, LAGA, Université Paris 13, 2004.

[3] E. BLAYO, L. HALPERN, AND C. JAPHET, *Optimized Schwarz waveform relaxation algorithms with nonconforming time discretization for coupling convection-diffusion problems with discontinuous coefficients*, in Domain decomposition methods in science and engineering XVI, vol. 55 of Lect. Notes Comput. Sci. Eng., Springer, Berlin, 2007, pp. 267–274.

[4] G. BRASSINGTON, M. MARTIN, H. TOLMAN, S. AKELLA, M. BALMESEDA, C. CHAMBERS, E. CHASSIGNET, J. CUMMINGS, Y. DRILLET, P. JANSEN, P. LALOYAUX, D. LEA, A. MEHRA, I. MIROUZE, H. RITCHIE, G. SAMSON, P. SANDERY, G. SMITH, M. SUAREZ, AND R. TODLING, *Progress and challenges in short- to medium-range coupled prediction*, J. Oper. Oceanogr., 8 (2015), pp. s239–s258.

[5] J. BYE, *Inertially coupled Ekman layers*, Dynam. Atmos. Oceans, 35 (2002), pp. 27–39.

[6] O. DUBOIS, M. J. GANDER, S. LOISEL, A. S.-C. A., AND B. DANIEL, *The optimized Schwarz method with a coarse grid correction*, SIAM J. Sci. Comput., 34 (2012), pp. A421–A458.

[7] T. DUNSTER, *Legendre and related functions*, in NIST handbook of mathematical functions hardback and CD-ROM, Cambridge University Press, 2010, ch. 14.

[8] V. EKMAN, *On the influence of the Earth's rotation in ocean-currents*, Arch. Math. Astron. Phys., 2 (1905), pp. 1–52.

[9] M. J. GANDER AND L. HALPERN, *Méthodes de relaxation d'ondes (SWR) pour l'équation de la chaleur en dimension 1*, Comptes Rendus Mathématique, 336 (2003), pp. 519 – 524.
[10] M. J. GANDER AND L. HALPERN, *Optimized Schwarz waveform relaxation methods for advection reaction diffusion problems*, SIAM J. Numer. Anal., 45 (2007), pp. 666–697 (electronic).
[11] M. J. GANDER, L. HALPERN, AND M. KERN, *A Schwarz waveform relaxation method for advection—diffusion—reaction problems with discontinuous coefficients and non-matching grids*, in Domain Decomposition Methods in Science and Engineering XVI, O. B. Widlund and D. E. Keyes, eds., Berlin, Heidelberg, 2007, Springer Berlin Heidelberg, pp. 283–290.
[12] M. J. GANDER, L. HALPERN, AND F. NATAF, *Optimal convergence for overlapping and non-overlapping Schwarz waveform relaxation*, in Proceedings of the 11th International Conference on Domain Decomposition Methods, C.-H. Lai, P. Bjørstad, M. Cross, and O. Widlund, eds., 1999.
[13] M. J. GANDER, Y.-L. JIANG, AND R.-J. LI, *Parareal Schwarz waveform relaxation methods*, in Domain Decomposition Methods in Science and Engineering XX, R. Bank, M. Holst, O. Widlund, and J. Xu, eds., Berlin, Heidelberg, 2013, Springer Berlin Heidelberg, pp. 451–458.
[14] M. J. GANDER, F. KWOK, AND B. C. MANDAL, *Dirichlet-Neumann and Neumann-Neumann waveform relaxation for the wave equation*, in Domain Decomposition Methods in Science and Engineering XXII, T. Dickopf, M. J. Gander, L. Halpern, R. Krause, and L. F. Pavarino, eds., Cham, 2016, Springer International Publishing, pp. 501–509.
[15] M. J. GANDER AND Y. XU, *Optimized Schwarz methods for model problems with continuously variable coefficients*, SIAM J. Sci. Comput., 38 (2016), p. A2964–A2986.
[16] B. GRISOGONO, *A generalized Ekman layer profile with gradually varying eddy diffusivities*, Quart. J. Roy. Meteorol. Soc., 121 (1995), pp. 445–453.
[17] D. E. KEYES ET AL., *Multiphysics simulations: Challenges and opportunities*, International Journal of High Performance Computing Applications, 27 (2013), pp. 4–83.
[18] F. LEMARIÉ, E. BLAYO, AND L. DEBREU, *Analysis of ocean-atmosphere coupling algorithms: Consistency and stability*, Procedia Computer Science, 51 (2015), pp. 2066 – 2075. International Conference On Computational Science, ICCS 2015.
[19] F. LEMARIÉ, L. DEBREU, AND E. BLAYO, *Toward an optimized global-in-time Schwarz algorithm for diffusion equations with discontinuous and spatially variable coefficients, part 1: The constant coefficients case*, Electron. Trans. Numer. Anal., 40 (2013), pp. 148–169.
[20] ———, *Toward an optimized global-in-time Schwarz algorithm for diffusion equations with discontinuous and spatially variable coefficients, part 2: the variable coefficients case*, Electron. Trans. Numer. Anal., 40 (2013), pp. 170–186.
[21] F. LEMARIÉ, L. DEBREU, G. MADEC, J. DEMANGE, J. MOLINES, AND M. HONNORAT, *Stability constraints for oceanic numerical models: implications for the formulation of time and space discretizations*, Ocean Modell., 92 (2015), pp. 124 – 148.
[22] D. LEWIS AND S. BELCHER, *Time-dependent, coupled, Ekman boundary layer solutions incorporating Stokes drift*, Dynam. Atmos. Oceans, 37 (2004), pp. 313–351.
[23] J. LIONS AND E. MAGENES, *Problèmes aux limites non homogènes et applications*, vol. 2, Dunod, 1968.
[24] P.-L. LIONS, *On the Schwarz alternating method. III. A variant for nonoverlapping subdomains*, in Third International Symposium on Domain Decomposition Methods for Partial Differential Equations (Houston,TX, 1989), SIAM, Philadelphia, PA, 1990, pp. 202–223.
[25] O. S. MADSEN, *A realistic model of the wind-induced Ekman boundary layer*, J. Phys. Oceanogr., 7 (1977), pp. 248–255.
[26] V. MARTIN, *Schwarz Waveform Relaxation Methods for oceanographic equations*, PhD thesis, Université Paris-Nord - Paris XIII, 2003.
[27] A. S. MONIN AND A. M. OBUKHOV, *Basic laws of turbulent mixing in the surface layer of the atmosphere*, Trudy Akademii Nauk SSSR Geofizicheskogo Instituta, 24 (1954), pp. 163–187.
[28] J. J. O'BRIEN, *A note on the vertical structure of the eddy exchange coefficient in the planetary boundary layer*, J. Atmos. Sci., 27 (1970), pp. 1213–1215.
[29] F. W. OLVER, *Hypergeometric function*, in NIST handbook of mathematical functions hardback and CD-ROM, Cambridge University Press, 2010, ch. 15.
[30] G. C. SMITH, J.-M. BÉLANGER, F. ROY, P. PELLERIN, H. RITCHIE, K. ONU, M. ROCH,

A. ZADRA, D. S. COLAN, B. WINTER, J.-S. FONTECILLA, AND D. DEACU, *Impact of coupling with an ice-ocean model on global medium-range NWP forecast skill*, Mon. Weather Rev., 146 (2018), pp. 1157–1180.
[31] G. K. VALLIS, *Atmospheric and Oceanic Fluid Dynamics: Fundamentals and Large-scale Circulation*, Cambridge University Press, 2006.

Appendix A. Quadratic viscosity basis functions. Eq. (3.1a) using the quadratic viscosity $\nu(z) = c+bz+az^2$ for $z \in \Omega$, can be reduced to the Legendre ODE $\left(1-\eta^2\right)\dfrac{\mathrm{d}^2 y}{\mathrm{d}\eta^2} - 2\eta\dfrac{\mathrm{d}y}{\mathrm{d}\eta} + \xi\left(\xi+1\right)y = 0$ with

$$\eta\left(z\right) = \frac{2a}{\sqrt{b^2-4ac}}\left(z+\frac{b}{2a}\right) \quad \text{and} \quad \xi = -\frac{1}{2}\left(1 \pm \sqrt{1+\frac{4\imath\left(f+\omega\right)}{a}}\right) \tag{A.1}$$

where the choice of the sign in (A.1) does not bear any consequence. In particular, one can show that using relevant quadratic viscosity functions, (e.g. satisfying $\nu(z) > 0$ for all $z \in \Omega$ and $(a,b,c) \in \mathbb{R}^*_- \times \mathbb{R}^2$), $\eta \in \mathbb{R}$ and satisfies $-1 < \eta(z) < 1$ for $z \in \Omega$. The functions given by (3.22) are then numerically satisfactory solutions to the Legendre ODE [meaning that computing a reasonable amount of sum terms leads to accurate values, 7], and thus to (3.1a). In our numerical results, Legendre functions have been computed using the hypergeometric function ${}_2F_1$ [29] through: $P^0_\xi\left(\eta\right) = {}_2F_1\left(\xi+1,-\xi,1;\eta\right)$.

Appendix B. On the observed discretized convergence factor. Let us consider the numerical solution of the coupled problem (1.3) on a given time window $\mathcal{T}_n$ using a finite difference discretization in time. The observed error can be written as (with $\mathbf{U}_j = (u_j, v_j)$):

$$\mathbf{E}_j^{k,m}(z) = \mathbf{U}_j^{k,m}(z) - \mathbf{U}_j(z,t_j^m) \qquad 1 \leq m \leq M_j, j \in \{1,2\}, k \in \mathbb{N}^* \tag{B.1}$$

where m is an index for the time step, t_j^m is the physical time corresponding to time step m, and M_j is the total number of time steps for the numerical approximation of $\mathbf{U}_j$ in $\mathcal{T}_n$. A convergence rate characterizing the behaviour of $\mathbf{E}_j^{k,m} = (E_{u,j}^{k,m}, E_{v,j}^{k,m})$ as a function of k is:

(B.2)

$$\rho^k_{\mathbf{U}_j} = \frac{\left\|\left(\mathbf{E}_j^{k,m}(0^\mp)\right)_m\right\|_2}{\left\|\left(\mathbf{E}_j^{k-1,m}(0^\mp)\right)_m\right\|_2} = \frac{\left[\sum\limits_{m=1}^{M_j}\left(\left(E_{u,j}^{k,m}(0^\mp)\right)^2 + \left(E_{v,j}^{k,m}(0^\mp)\right)^2\right)\right]^{1/2}}{\left[\sum\limits_{m=1}^{M_j}\left(\left(E_{u,j}^{k-1,m}(0^\mp)\right)^2 + \left(E_{v,j}^{k-1,m}(0^\mp)\right)^2\right)\right]^{1/2}} \qquad k \in \mathbb{N}^*, j \in \{1,2\}$$

At a continuous the errors on the complex variables $(\varphi, \overline{\varphi})$ are:

$$\mathbf{e}_j^{k,m}(z) = \begin{pmatrix} e_{\varphi,j}^{k,m}(z) \\ e_{\overline{\varphi},j}^{k,m}(z) \end{pmatrix} = \begin{pmatrix} \varphi_j^{k,m}(z) - \varphi(z,t_m^j) \\ \overline{\varphi}_j^{k,m}(z) - \overline{\varphi}(z,t_m^j) \end{pmatrix} \tag{B.3}$$

where $\varphi_j^{k,m}$ and $\overline{\varphi}_j^{k,m}$ are defined by the Schwarz algorithm (2.5). $\mathbf{E}_j^{k,m}$ is linked to $\mathbf{e}_j^{k,m}$ by:

$$\mathbf{E}_j^{k,m} = \mathbf{P}\mathbf{e}_j^{k,m} = \frac{1}{\sqrt{2}}\begin{pmatrix} e_{\varphi,j}^{k,m} + e_{\overline{\varphi},j}^{k,m} \\ -\imath e_{\varphi,j}^{k,m} + \imath e_{\overline{\varphi},j}^{k,m} \end{pmatrix} \tag{B.4}$$

where $\mathbf{P}$ is given in Sec. 2.1. Since $\mathbf{P}$ is a unitary matrix (i.e. $\mathbf{P}^{-1} = \overline{\mathbf{P}}^T$),

$$\left\|\mathbf{E}_j^{k,m}\right\|_2^2 = \left(\bar{\mathbf{e}}_j^{k,m}\right)^T \overline{\mathbf{P}}^T \mathbf{P} \mathbf{e}_j^{k,m} = \left(\bar{\mathbf{e}}_j^{k,m}\right)^T \mathbf{e}_j^{k,m} = \left\|\mathbf{e}_j^{k,m}\right\|_2^2 \tag{B.5}$$

meaning that (B.2) becomes

$$\rho_{\mathbf{U}_j}^k = \frac{\left[\sum_{m=1}^{M_j}\left(\left(e_{\varphi,j}^{k,m}(0^{\mp})\right)^2 + \left(e_{\overline{\varphi},j}^{k,m}(0^{\mp})\right)^2\right)\right]^{1/2}}{\left[\sum_{m=1}^{M_j}\left(\left(e_{\varphi,j}^{k-1,m}(0^{\mp})\right)^2 + \left(e_{\overline{\varphi},j}^{k-1,m}(0^{\mp})\right)^2\right)\right]^{1/2}} \qquad k \in \mathbb{N}^*, j \in \{1,2\} \tag{B.6}$$

Let us now define $\widetilde{\rho}_{\varphi,j}^{k,M_j} = \frac{\left\|\left(e_{\varphi,j}^{k,m}(z=0^{\mp})\right)\right\|_2}{\left\|\left(e_{\varphi,j}^{k-1,m}(z=0^{\mp})\right)\right\|_2} = \frac{\left[\sum_{m=1}^{M_j}\left(e_{\varphi,j}^{k,m}(0^{\mp})\right)^2\right]^{1/2}}{\left[\sum_{m=1}^{M_j}\left(e_{\varphi,j}^{k-1,m}(0^{\mp})\right)^2\right]^{1/2}}$ for $k \in \mathbb{N}^*, j \in \{1,2\}$. When $M_j \to +\infty$ (i.e. simulating (2.5) on a infinite time window), the temporal grid can only generate modes which frequencies lie in $I_\omega := \left[-\frac{\pi}{\min\limits_{j\in\{1,2\}}\{\delta t_j\}}; \frac{\pi}{\min\limits_{j\in\{1,2\}}\{\delta t_j\}}\right]$. This is due to the Nyquist-Shannon sampling theorem [6]. $\widehat{\left(e_{\varphi,j}^{k,m}(0^{\mp})\right)}$ corresponds to the Fourier transform of the continuous error $\hat{e}_\varphi^k$ on I_ω. The convergence factor denoted $\widetilde{\rho}_{\varphi,j}^{k,\infty}$ can be linked to the errors in the Fourier space by the Parseval's theorem:

$$\widetilde{\rho}_{\varphi,j}^{k,\infty} = \frac{\left[\sum_{m=1}^{\infty}\left(e_{\varphi,j}^{k,m}(0^{\mp})^2\right]^{1/2}\right.}{\left[\sum_{m=1}^{\infty}\left(e_{\varphi,j}^{k-1,m}(0^{\mp})^2\right]^{1/2}\right.} = \frac{\left(\int_{\omega\in I}\left(\rho_{\varphi,j}^k(\omega)\right)^2\left|\hat{e}_{\varphi,j}^{k-1}(\omega)\right|^2 d\omega\right)^{1/2}}{\left(\int_{\omega\in I}\left|\hat{e}_{\varphi,j}^{k-1}(\omega)\right|^2 d\omega\right)^{1/2}}$$

which implies that $\inf\limits_{|\omega|\leq\pi/\min\limits_{j\in\{1,2\}}\{\delta t_j\}} \rho_{\varphi,j}^k(\omega), \leq \widetilde{\rho}_{\varphi,j}^{k,\infty} \leq \sup\limits_{|\omega|\leq\pi/\min\limits_{j\in\{1,2\}}\{\delta t_j\}} \rho_{\varphi,j}^k(\omega)$. Moreover, using the identity $\sum_{m=1}^{M_j} x_m = \left(\sum_{m=1}^{\infty} x_m\right)\left(1 - \left\{\sum_{m=M_j+1}^{\infty} x_m\right\} / \left\{\sum_{m=1}^{\infty} x_m\right\}\right)$, $\widetilde{\rho}_{\varphi,j}^{k,M_j}$ can easily be linked to $\widetilde{\rho}_{\varphi,j}^{k,\infty}$:

$$\left(\widetilde{\rho}_{\varphi,j}^{k,M_j}\right)^2 = \left(\widetilde{\rho}_{\varphi,j}^{k,\infty}\right)^2 \frac{1-\Gamma_{\varphi,j}^{k,M_j}}{1-\Gamma_{\varphi,j}^{k-1,M_j}} \qquad \text{with } \Gamma_{\varphi,j}^{k,M_j} = \frac{\sum_{m=M_j+1}^{\infty}\left(e_{\varphi,j}^{k,m}(0^{\mp})\right)^2}{\sum_{m=1}^{\infty}\left(e_{\varphi,j}^{k,m}(0^{\mp})\right)^2} \tag{B.7}$$

Since $\Gamma_{\varphi,j}^{k,M_j} \longrightarrow 0$ as $M_j \to \infty$ (thanks to §2.3), (B.7) can be rewritten as $\widetilde{\rho}_{\varphi,j}^{k,M_j} = \widetilde{\rho}_{\varphi,j}^{k,\infty} + \mathcal{O}\left(\Gamma_{\varphi,j}^{k,M_j}\Gamma_{\varphi,j}^{k-1,M_j}\right)$. Finally the same relationships being true for $e_{\overline{\varphi},j}^{k,m}$, we end up with:

$$\rho_{\mathbf{U}_j}^k \leq \max\left\{\sup_{|\omega|\leq\pi/\min\limits_{j\in\{1,2\}}\{\delta t_j\}} \rho_{\varphi,j}^k(\omega), \sup_{|\omega|\leq\pi/\min\limits_{j\in\{1,2\}}\{\delta t_j\}} \rho_{\overline{\varphi},j}^k(\omega)\right\} + \epsilon \tag{B.8}$$

Appendix C. Proof for the upper bound (4.7). In this appendix we provide the proof for the upper bound (4.7) on $\rho_{\rm DN}^{\rm cst}$ for constant viscosity and Dirichlet-Neumann interface conditions given in Sec. 4.3. We first reformulate $\rho_{\rm DN}^{\rm cst}$ as $\rho_{\rm DN}^{\rm cst} = \sqrt{\lambda}\sqrt{\frac{\mathcal{Q}(\sqrt{2{\rm Fo}_2})}{\mathcal{Q}(\sqrt{2{\rm Fo}_1})}}$ with

$$\mathcal{Q}(x) = \frac{\cosh x - \cos x}{\cosh x + \cos x}$$

C.1. Proof for the upper bound (4.7) for ${\rm Fo}_2 < {\rm Fo}_1$. The derivative of $\mathcal{Q}(x)$ cancels for $x^\star$ such that $\tanh(x^\star)+\tan(x^\star) = 0$. This transcendental equation has no root on $[0, \pi/2]$ (and $0 \leq \mathcal{Q}(x) \leq 1$ on that interval) and then one root $x^{(\star,k)}$ per interval $[\pi/2 + k\pi, 3\pi/2 + k\pi]$ ($k \geq 0$). For even values of k, $\mathcal{Q}(x^{(\star,k)})$ is a local maximum and $\mathcal{Q}(x) \geq 1$, while for odd values of k, $\mathcal{Q}(x^{(\star,k)})$ is a local minimum and $\mathcal{Q}(x) \leq 1$. Moreover it can be shown that $\mathcal{Q}(x^{(\star,0)}) > \mathcal{Q}(x^{(\star,2)}) > \mathcal{Q}(x^{(\star,4)}) > \ldots > 1$ and $\mathcal{Q}(x^{(\star,1)}) < \mathcal{Q}(x^{(\star,3)}) < \mathcal{Q}(x^{(\star,5)}) < \ldots < 1$. This implies that the maximum of $\mathcal{Q}(x)$ is $\mathcal{Q}(x^{(\star,0)})$ and thus that

$$\mathcal{Q}(x) \leq \mathcal{Q}(x^{(\star,0)}), \qquad x \geq 0$$

If we now introduce $\alpha = \sqrt{{\rm Fo}_2/{\rm Fo}_1}$ and consider $x = \sqrt{2{\rm Fo}_1}$, our problem is to find the upper bound of $\frac{\mathcal{Q}(\alpha x)}{\mathcal{Q}(x)}$ with $\alpha \leq 1$ (because we consider the case ${\rm Fo}_2 < {\rm Fo}_1$ here). It is straightforward to prove that $\mathcal{Q}(\alpha x) \leq \mathcal{Q}(x^{(\star,0)})$, for $x \geq 0, \alpha \leq 1$ and $\mathcal{Q}(\alpha x)$ behaves like $\mathcal{Q}(x)$ on the subintervals $[\frac{\pi}{2\alpha} + k\pi, \frac{3\pi}{2\alpha} + k\pi]$. We can then proceed sub-interval by sub-interval: (*i*) on $[0, \pi/2]$ $\mathcal{Q}(x)$ increases more rapidly than $\mathcal{Q}(\alpha x)$. We thus have $\frac{\mathcal{Q}(\alpha x)}{\mathcal{Q}(x)} \leq 1$ as soon as $\alpha \leq 1$; (*ii*) on $[\pi/2, 3\pi/2]$ $\mathcal{Q}(x)$ is larger than 1, meaning that $\frac{1}{\mathcal{Q}(x)} \leq 1$. We thus have $\frac{\mathcal{Q}(\alpha x)}{\mathcal{Q}(x)} \leq \mathcal{Q}(x^{(\star,0)})$ whatever the value of α; (*iii*) on $[3\pi/2, 5\pi/2]$ $\mathcal{Q}(x)$ has a local minimum $\mathcal{Q}(x^{(\star,1)})$ which is smaller than 1. We thus have $\frac{1}{\mathcal{Q}(x)} \leq \frac{1}{\mathcal{Q}(x^{(\star,1)})}$ and the worse case scenario is when this coincides with values of α such that the maximum of $\mathcal{Q}(\alpha x)$ occurs for $x \in [3\pi/2, 5\pi/2]$. We thus obtain:

$$\frac{\mathcal{Q}(\alpha x)}{\mathcal{Q}(x)} \leq \frac{\mathcal{Q}(x^{(\star,0)})}{\mathcal{Q}(x^{(\star,1)})}$$

Because of the ordering of the values $\mathcal{Q}(x^{(\star,k)})$ given earlier (i.e. $\mathcal{Q}(x^{(\star,k)})$ gets closer and closer to 1 as k increases), it is not needed to go beyond $x = 5\pi/2$ since the upper bound could not be larger for $x > 5\pi/2$.

C.2. Proof for the upper bound (4.7) for ${\rm Fo}_2 \geq {\rm Fo}_1$. For this proof, we first study the behaviour of $\frac{\mathcal{Q}(x)}{x^2}$. The sign of the derivative of $\frac{\mathcal{Q}(x)}{x^2}$ with respect to x is the same as

$$\cos^2(x) - \cosh^2(x) + x(\cosh(x)\sin(x) + \sinh(x)\cos(x))$$

which is smaller or equal to zero for $x \geq 0$, $\frac{\mathcal{Q}(x)}{x^2}$ is thus a decreasing function of x for $x \geq 0$. In the case $\alpha \geq 1$ (i.e. ${\rm Fo}_2 \geq {\rm Fo}_1$) we have $\alpha x \leq x$, hence $\dfrac{\mathcal{Q}(\alpha x)}{\alpha^2 x^2} \leq \dfrac{\mathcal{Q}(x)}{x^2}$ which leads to $\dfrac{\mathcal{Q}(\alpha x)}{\mathcal{Q}(x)} \leq \alpha^2$ where $x = \sqrt{2{\rm Fo}_1}$ and $\alpha = \sqrt{{\rm Fo}_2/{\rm Fo}_1}$. We can rewrite this last inequality in terms of ${\rm Fo}_j$ to obtain

$$\rho_{\rm DN}^{\rm cst} \leq \sqrt{\lambda \frac{{\rm Fo}_2}{{\rm Fo}_1}} \tag{C.1}$$

Note that this also proves that $|\mathcal{S}_2^{\rm cst}({\rm Fo})|$ decreases, and thus $|\mathcal{S}_2^{\rm cst}({\rm Fo})| \geq \left|\mathcal{S}_2^{\rm sta,cst}\right| = |h_2|$. Similarly, $|\mathcal{S}_1^{\rm cst}({\rm Fo})|$ increases and $|\mathcal{S}_1^{\rm cst}({\rm Fo})| \leq \left|\mathcal{S}_1^{\rm sta,cst}\right| = |h_1|^{-1}$.